
جامعة الملك عبدالله
للعلوم والتقنية
King Abdullah University of
Science and Technology

Efficient and stable perovskite-silicon tandem solar cells through contact displacement by MgF x

Item Type	Article
Authors	Liu, Jiang; de Bastiani, Michele; Aydin, Erkan; Harrison, George T; Gao, Yajun; Pradhan, Rakesh R.; Eswaran, Mathan Kumar; Mandal, Mukunda; Yan, Wenbo; Seitkhan, Akmaral; Babics, Maxime; Subbiah, Anand Selvin; Ugur, Esma; Xu, Fuzong; Xu, Lujia; Wang, Mingcong; Rehman, Atteq Ur; Razzaq, Arsalan; Kang, Jingxuan; Azmi, Randi; Said, Ahmed Ali; Isikgor, Furkan Halis; Allen, Thomas; Andrienko, Denis; Schwingenschlögl, Udo; Laquai, Frédéric; De Wolf, Stefaan
Citation	Liu, J., De Bastiani, M., Aydin, E., Harrison, G. T., Gao, Y., Pradhan, R. R., Eswaran, M. K., Mandal, M., Yan, W., Seitkhan, A., Babics, M., Subbiah, A. S., Ugur, E., Xu, F., Xu, L., Wang, M., Rehman, A. ur, Razzaq, A., Kang, J., ... De Wolf, S. (2022). Efficient and stable perovskite-silicon tandem solar cells through contact displacement by MgF x . Science. https://doi.org/10.1126/science.abn8910
Eprint version	Post-print
DOI	10.1126/science.abn8910
Publisher	American Association for the Advancement of Science (AAAS)
Journal	Science
Rights	Archived with thanks to Science
Download date	28/09/2023 02:39:12

Link to Item	http://hdl.handle.net/10754/679342

Submitted Manuscript: Confidential
Template revised February 2021

Efficient and stable perovskite-silicon tandem solar cells through contact displacement by MgF_x

Jiang Liu[1]*, Michele De Bastiani[1], Erkan Aydin[1], George T. Harrison[1], Yajun Gao[1], Rakesh R. Pradhan[1], Mathan K. Eswaran[1], Mukunda Mandal[2], Wenbo Yan[1], Akmaral Seitkhan[1], Maxime Babics[1], Anand S. Subbiah[1], Esma Ugur[1], Fuzong Xu[1], Lujia Xu[1], Mingcong Wang[1], Atteq ur Rehman,[1] Arsalan Razzaq[1], Jingxuan Kang[1], Randi Azmi[1], Ahmed Ali Said[1], Furkan H. Isikgor[1], Thomas G. Allen[1], Denis Andrienko[2], Udo Schwingenschlögl[1], Frédéric Laquai[1], Stefaan De Wolf[1]*

[1]King Abdullah University of Science and Technology (KAUST), KAUST Solar Center (KSC), Physical Sciences and Engineering Division (PSE); Thuwal 23955-6900, Kingdom of Saudi Arabia
[2]Max Planck Institute for Polymer Research, 55128 Mainz, Germany

*Corresponding author. Email: jiang.liu@kaust.edu.sa; stefaan.dewolf@kaust.edu.sa

Abstract:

The performance of perovskite solar cells with inverted polarity (*p-i-n*) is still limited by recombination at their electron extraction interface, which also lowers the power conversion efficiency (PCE) of *p-i-n* perovskite-silicon tandem solar cells. A ~1 nm thick MgF_x interlayer at the perovskite/C_{60} interface through thermal evaporation favorably adjusts the surface energy of the perovskite layer, facilitating efficient electron extraction, and displaces C_{60} from the perovskite surface to mitigate nonradiative recombination. These effects enable a champion V_{oc} of 1.92 volts, an improved fill factor of 80.7%, and an independently certified stabilized PCE of 29.3% for a ~1 square centimeter monolithic perovskite-silicon tandem solar cell. The tandem retained ~95% of its initial performance following damp-heat testing (85 Celsius at 85% relative humidity) for > 1000 hours.

One Sentence Summary: Magnesium fluoride interlayer reduces interface recombination and enables a certified 29.3% efficient monolithic perovskite/silicon tandem solar cell.

Main Text:

Integrating high-performance wide-bandgap perovskite solar cells onto silicon solar cells can lead to very high power conversion efficiencies (PCEs) by minimizing carrier-thermalization losses (*1-6*). Although initial research explored *n-i-p* tandems, recent works have focused on the *p-i-n* configuration, in which the *n*-type electron-collecting contact faces sunward (*7-9*), and on improving performance through device optics and optimizing perovskite composition (*10-15*). More recently, attention turned to the interface between the perovskite and the hole transport layer (HTL) to reduce voltage losses. Approaches include molecular passivation of NiO_x (*16, 17*) and the use of self-assembled monolayers (SAMs) such as 2PACz and Me-4PACz, anchored on oxides, to reduce V_{oc} losses (*18, 19*).

Despite this progress, state-of-art PSCs, especially those incorporating wider-bandgap perovskites (e.g. ~1.68 eV as frequently used for tandem applications), have an undesirably large V_{oc} deficit when compared to the theoretical radiative limit. This problem mainly stems from substantial charge carrier recombination and an energy level mismatch at the perovskite interface with the electron transport layer (ETL) (*20-22*), which most commonly consists of evaporated C_{60}. Inserting an ultrathin LiF layer at the perovskite/C_{60} interface alleviates this issue to a certain extent, yet this may result in reduced device stability, usually attributed to the deliquescent behavior and high ion diffusivity of Li salts (*19, 23-25*). Two-dimensional (2D) perovskites and some fullerene derivatives prepared by solution processes have been previously used to passivate the perovskite/C_{60} rear interface in single-junction *p-i-n* PSCs (*26, 27*). However, in the *p-i-n* tandem configuration, the perovskite/C_{60} interface faces sunwards, which demands interfacial layers with a high transparency, high stability and good thickness control. To this end, we systematically investigated alternative evaporated metal fluorides (such as NaF, CaF_x, and MgF_x) as interlayer at the perovskite/C_{60} interface. We demonstrated that the charge transport and recombination interfaces could be carefully tuned with MgF_x interlayers, enabling a certified stabilized PCE of 29.3%.

We fabricated monolithic perovskite-silicon tandem solar cells from silicon heterojunction (SHJ) bottom cells using crystalline silicon (c-Si) wafers with double-side texture (Fig. 1A) to reduce the front reflection and improve light trapping in our devices (*8, 16*). We verified the ultrathin nature of the fluoride-based interlayers, inserted at the electron-selective top contact, with cross-sectional high-resolution scanning transmission electron microscopy (HR-STEM, Fig. 1B and figures S1 and S2). The magnified STEM images and energy-dispersive X-ray (EDX) spectroscopy mapping clearly outline the perovskite/MgF_x/C_{60}/SnO_2/IZO top contact structure, identifying the presence of a ~15 nm C_{60} layer and a ~20 nm SnO_2 layer. The latter acts as a buffer against damage from sputtering of the indium zinc oxide (IZO) transparent top electrode (*28*). We note that after perovskite deposition, all subsequently deposited films were obtained by vapor deposition techniques that yield highly accurate and reproducible layer thicknesses. For instance, because the fluoride-based film is thermally evaporated, the resulting interlayer is highly uniform in thickness, less affected by the surface roughness of the underlying perovskite, contrasting with typical solution-processed interlayers (*27*).

We investigated the energy-level alignment of our perovskite layers with LiF, NaF, CaF_x and MgF_x overlayers by ultraviolet photoemission spectroscopy (UPS) and low-energy inverse photoemission spectroscopy (LE-IPES) for occupied and unoccupied states, respectively. As shown in Fig. 1C, the work function (*WF*) of the bare perovskite is ~4.97 eV. By coating the perovskite with a thin fluoride-based layer, the *WF* systematically shifts toward smaller values.

Both MgF_x and CaF_x caused a larger *WF* shift than did LiF and NaF did (Fig. 1C and Fig. S3). With the presence of metal fluoride interlayers, the valence band maximum (*VBM*) of the perovskite, determined with a Gaussian fitting method (*29*), was lowered relative to its Fermi level (E_F), implying that the metal fluorides caused a downward band bending at the perovskite interface that favored electron extraction.

Kelvin probe force microscopy (KPFM) measurements, conducted in an ambient environment, confirmed the trend of the UPS results (Fig. S4) (*30*), that is, the MgF_x and CaF_x samples displayed a larger *WF* shift compared to LiF and NaF ones (Fig. S5). To further evaluate such band bending as a function of ETL thickness, we conducted additional UPS/LE-IPES measurements (Fig. S6 and S7) that allowed us to map out the band structure at the perovskite/ETL interface. The perovskite/C_{60} sample displayed negligible band bending (Fig. S6), which is consistent with previous work on the $MAPbI_3/C_{60}$ interface (*31*). However, the presence of a MgF_x interlayer led to energy band bending at the perovskite surface (Fig. 1D). Also, the lowest unoccupied molecular orbital (LUMO) of the C_{60} layer bent down toward the perovskite interface, which implied that the MgF_x layer promoted the formation of electron-selective contacts with low interfacial resistance (*32*).

Moreover, the MgF_x interlayer also displaced C_{60} from the perovskite surface, thus suppressing interface recombination (see below). The thinness of the metal fluoride interlayer with a thickness of 0.5~1.5 nm ensures that collected electrons can reach the LUMO of the C_{60} layer through quantum-mechanical tunneling or via pinholes, thus enabling the selective extraction of electrons Once the electrons transferred to C_{60}, they became the majority charge carriers and were easily transported through the C_{60} layer and collected by the SnO_2/IZO transparent electrode. Furthermore, X-ray photoelectron spectroscopy (XPS) results (Fig. S8) showed that the evaporated ultrathin (~1 nm) MgF_x films strongly deviated from their bulk stoichiometric (x=2) composition, with an x value in the range 1.0±0.2. We expect this substoichiometric nature to produce a transverse electric dipole in this layer that promotes electron extraction.

To evaluate enhanced contact passivation with fluoride interlayers, we quantified the non-radiative recombination losses at the perovskite/ETL interfaces through absolute photoluminescence (PL) imaging under 1-sun equivalent illumination. This method let us extract the quasi-Fermi-level splitting (*QFLS* or Δμ) in the perovskite layer, which relates to the upper limit voltage of complete devices (*33, 34*). Fig. 2A and Fig. S9 showed that the mean *QFLS* of IZO/2PACz/perovskite structures without ETL was ~1.285 eV, whereas the IZO/2PACz/perovskite/C_{60} sample exhibited a sharp decline of *QFLS* with a mean value of 1.179 eV. The LiF- and MgF_x-treated samples display *QFLS* values of 1.198 and 1.217 eV, respectively. The HTL side remained unchanged, so we associated the undesired lower *QFLS* with trap-assisted recombination at the perovskite/ETL interface. Structural disorder or molecular imperfections in fullerene-based ETLs commonly have a strong band tail state (*35, 36*) that may interact electronically with the perovskite layer to form undesired recombination channels.

Time-resolved photoluminescence (TRPL) spectroscopy further revealed that the IZO/2PACz/perovskite structure supported a very slow carrier decay process with an average carrier lifetime of ~1.6 μs (Fig. 2B and Table S1). Coating C_{60} directly onto the perovskite expectedly caused a large reduction in PL lifetime to 26 ns, but the use of a MgF_x interlayer prolonged the average PL decay time to 83 ns, compared to 38 ns for the perovskite/C_{60} sample.

Transient absorption spectroscopy (TAS, see Fig. S11) revealed a sharp negative band peaking at 718 and 710 nm for bare and C_{60}-coated perovskite samples, respectively, that could be assigned to ground-state photobleaching. As expected, the TAS signals of the perovskite/C_{60} sample exhibited faster decay of the bleaching peak than their perovskite/MgF_x/C_{60} counterparts. By globally fitting the TA decay curves of the three samples under four laser excitation conditions to a diffusion equation (Fig. S10), we obtained a first-order charge-carrier decay constant k_1 of 3.48×10^5 s^{-1} ($1/k_1\approx2.87$ μs). This value was consistent with our PL decay and the electron-hole diffusion length of ~12 μm, which is much longer than perovskite thickness, as desired for efficient solar cells.

These result indicate that the trap states causing nonradiative recombination mainly reside at the perovskite/ETL interface. To investigate the origin of these traps, we conducted density functional theory (DFT) calculations with the structural model of the perovskite/C_{60} interface shown in Fig 2C. The density of states (DOS) calculated at the relaxed contact distance showed the formation of deep trap states within the perovskite bandgap (inset, Fig. 2C). Similar calculations on prototypical $FAPbI_3$ perovskite confirmed the formation of such induced states (Fig. S12). Notably, these states are not created by defects in the perovskite but are induced by proximity with C_{60} and are similar to metal-induced gap states in metal/semiconductor contacts (*37, 38*). The MgF_x interlayer displaced C_{60} away from the perovskite and suppressed the induced trap states. Based on these findings, we argue that a key role of the interlayers is the blocking of the gap-state assisted recombination channels, thus suppressing charge recombination at the perovskite/ETL interface. In addition, DFT calculations showed that without interlayers, partial electron transfer from the perovskite into the C_{60} (Fig. S16) created a barrier for electron extraction.

To verify improved charge extraction at the perovskite/C_{60} interface, we fabricated single-junction *p-i-n* devices with metal fluoride-based interlayers, as well as control samples without interlayer. The solar cell with a MgF_x contact displacer reached a V_{oc} of 1.23 V, representing a ~50 mV absolute enhancement when compared to the control (Fig. S17) and a ~20 mV enhancement versus a LiF interlayer. These results agreed well with our energy-level and surface-passivation analyses. Notably, the *FF* improved to 81.1%, which we attributed to enhanced charge extraction and suppressed interface recombination at maximum-power point conditions. In addition, we tested CaF_x devices and found they also show remarkable V_{oc} and *FF*, implying that the alkali-earth metal fluoride as a contact displacer is a generic route to improve device performance.

We fabricated monolithic perovskite/silicon tandem solar cells using double-textured Si bottom cell with a sub-micrometer random pyramid structure (Fig. S19). The MgF_x-based device showed a remarkable reverse-scan *PCE* of up to 30.5% with a short-circuit current density, J_{sc} of 19.8 mA/cm^2, a V_{oc} of 1.92 V, and a *FF* of 80.7% (Fig. 3A). The control tandem showed a best *PCE* of 28.6% with a J_{sc} of 19.8 mA/cm^2, a V_{oc} of 1.85 V, an *FF* of 77.9% under reverse scan. The device statistics (Fig. 3, B and C, and Fig. S20) corroborated that the *PCE* improvement was mainly the result of enhanced V_{oc} and *FF*. One unencapsulated MgF_x-based tandem was certified at Fraunhofer ISE CalLab, showed a reverse-scan *PCE* of 29.4% with a J_{sc} of 19.8 mA/cm^2, a V_{oc} of 1.91 V, an *FF* of 77.6%, and a steady-state *PCE* of 29.3% (Fig. 3D or Fig. S21). Integrating the calibrated *EQE* (Fig. 3E) over the AM1.5G spectrum yielded J_{sc} values of 20.0 and 19.8 mA/cm^2 for the perovskite and c-Si subcells, respectively, which agreed with our tandem J_{sc} values of ~19.8 mA/cm^2. Our optical analysis revealed that the optical loss, in addition to some reflection, mainly came from parasitic absorption in the IZO transparent top electrode and C_{60} layer (Fig. S22), which accounted for equivalent values of 0.64 and 0.62 mA/cm^2, respectively.

To evaluate the perovskite subcell device performance, we conducted electroluminescence (EL) measurements on tandem devices. With an injected current of 22 mA/cm^2, we observed well-resolved EL spectral mapping with peaks positioning at ~735 nm (Fig. 3F and 3G), corresponding to the perovskite bandgap energy of ~1.69 eV. Under any current injection condition, the MgF_x-based tandem showed a relatively higher EL emission intensity than the control device, indicating a higher internal voltage (Fig. S24). Combining the EL spectra results of the perovskite subcell under distinct current injection conditions with Suns-V_{oc} data of the c-Si single-junction cell, we constructed so-called pseudo *J-V* curves of our perovskite/silicon tandem (Fig. 3H), free of any series resistance (R_s) losses. For the MgF_x-based tandem, we obtained a pseudo-V_{oc} of 1.93 V which is remarkably near the V_{oc} of 1.92 V from standard *J-V* measurements. A pseudo-FF of 84.8% and pseudo-PCE of 32.5% could be also estimated, implying that ~3% in absolute *PCE* was lost to series resistance.

We explored the effect of the interlayer on device stability by monitoring the photovoltaic performance of the control and fluoride-based tandems without encapsulation under continual standard AM1.5G illumination (Fig. 4A). The control device benefitted from light soaking in that its *PCE* increased from initially 27.2% to 28.0% after 10 min of illumination. The *J-V* curves (Fig. S26) demonstrated that the light soaking improved V_{oc} and *FF*; we speculate that continuous illumination caused a slight favorable adjustment of the energy alignment at the perovskite/ETL interface. The fluoride-based devices did not appear to benefit from this (Fig. 4B and Fig. S26), possibly because of the improved energy-level alignment at their perovskite/ETL interface. On a longer timescale, the LiF-based tandem, reputed for low stability (*19*), showed a gradual performance drop from 29.1% to 27.5% in air, whereas the MgF_x-based tandem retained nearly >99% of its initial *PCE* after 260 min, which we attribute to MgF_x being non-hygroscopic and having a lower metal ion diffusivity. The control device maintained relatively stable but still lower absolute V_{oc} and *FF* values after the light-soaking period, compared to MgF_x-based devices.

In addition, we subjected our encapsulated tandem device to damp-heat testing (85 ^{o}C with 85% relative humidity, RH, IEC 61215:2021 standard, Fig. 4C and Fig. S27). The MgF_x-treated tandem device did not show any V_{oc} or J_{sc} degradation after over 1000 hours, and retained 95.4% of its initial *PCE*. The V_{oc} even improved slightly, indicating that the perovskite itself and the interfacial layers were sufficiently tolerant to thermal stress. The *FF* showed a slight drop, which may be related to the increase in the series resistance of the contact electrode. In contrast, the LiF-treated tandem showed an obvious drop in *PCE* after an initial 125-hour testing (Fig. 4C and Fig. S27). These results indicated that our MgF_x-tandem devices, with a reasonable encapsulation scheme, could pass the damp-heat test protocol of the IEC 61215:2021 standard.

Acknowledgments: We acknowledge the use of KAUST Solar Center and Core Lab facilities and the support from its staff.
Funding: This work was supported by the King Abdullah University of Science and Technology (KAUST) under Award No: OSR-CARF/CCF-3079, OSR-CRG2019-4093, OSR-CRG2020-4350, IED OSR-2019-4208, IED OSR-2019-4580, and REI/1/4833-01-01.

Author contributions:

Conceptualization: JL, EA, SDW

Methodology: JL, MDB, YG, GTH, RRP, MKE, MM, AS, EA, LX

Investigation: JL, MDB, YG, GTH, RRP, MKE, MM, AS, WY, FX, LX, AuR, AR, TGA, MW, JK, AAS

Visualization: JL, GTH, RRP, MKE, MM, AS, YG, ASS, EU, MW

Funding acquisition: SDW, FL, DA, US

Supervision: SDW, FL, DA, US

Writing – original draft: JL, EA, SDW

Writing – review & editing: JL, SDW, EA, EU, MDB, FL, YG, GTH, FHI, RA

Competing interests: "J.L. and S.D.W. are inventors on patent application (63/312,896) submitted by King Abdullah University of Science and Technology that covers the alkali-earth metal fluoride used in this work."

Data and materials availability: All data are available in the main text or the supplementary materials.

Supplementary Materials

Materials and Methods

Supplementary Text

Fig. S1 to S27

Tables S1

References (39-56)

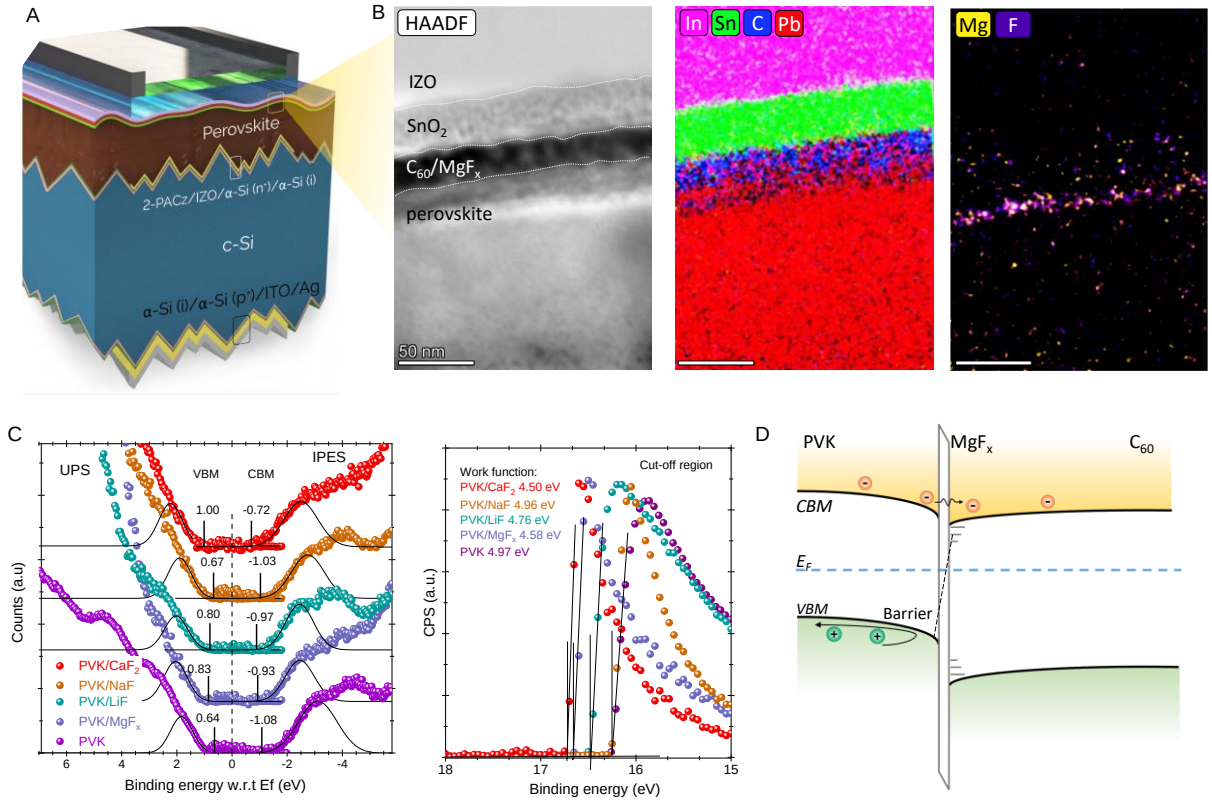

Fig. 1. Interface structure and electronic properties. (A) Schematic of the monolithic perovskite/silicon tandem solar cell built from a double-side textured silicon heterojunction cell. (B) Cross-sectional HR-STEM image and the corresponding energy-dispersive X-ray (EDX) mapping at the ETL-side. (C) Valence band (VB) and photoelectron cut-off region of the perovskite, and perovskite/1 nm-interlayer using UPS and IPES spectra. All samples were deposited on IZO/2PACz coated c-Si substrates. (D) Energy level diagram of the perovskite/C_{60} interface with MgF_x insertion layer.

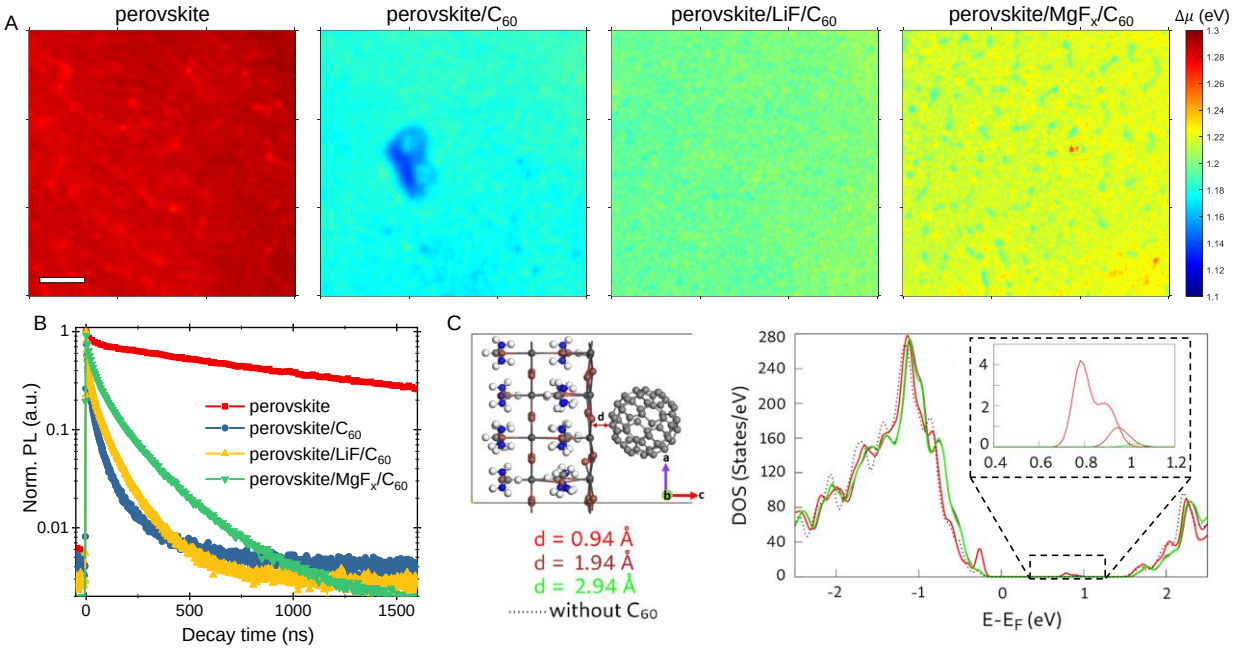

Fig. 2. Photoluminescence and transient absorption spectra. (A) Quasi-Fermi level splitting (*QFLS*) mapping for the perovskite, perovskite/C_{60}, perovskite/LiF/C_{60}, and perovskite/MgF_x/C_{60} samples on 2PACz-coated Si cell under 1 sun equivalent light intensity. The scale bar is 50 μm. (B) Time-resolved photoluminescence (TRPL) spectra of the bare perovskite and the perovskite films coated with different ETL structures. (C) Schematic model and DOS of a wide-bandgap perovskite as a function of the distance *d* to the C_{60} molecule. The inset of the enlarged DOS shows the induced midgap states when C_{60} is in close proximity to perovskite.

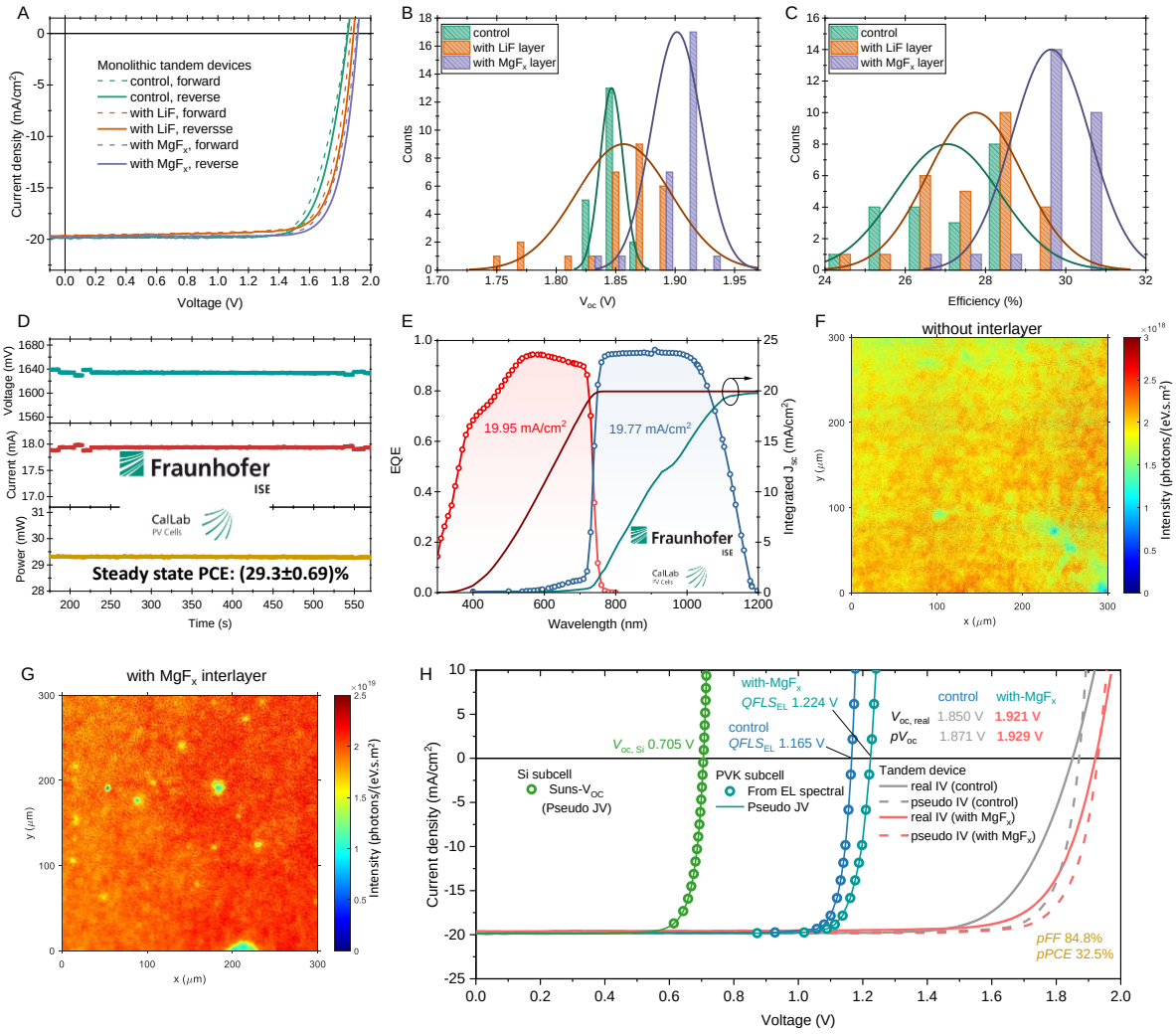

Fig. 3. Photovoltaic performances and Pseudo JV characteristics stability tests. (A) J-V curves of the champion tandem cell. (B, C) Histogram of V_{oc} (B) and *PCE* (C) for the tandem solar cells fabricated in this study. (D) Stabilized power output of one MgF_x-based tandem device, certified by Fraunhofer ISE CalLab. (E) EQE spectra of the certified tandem device. (F, G) Absolute EL mapping of perovskite subcell without and with MgF_x interlayer under 22 mA/cm^2 injection current. (H) Reconstructed pseudo JV characteristics of our tandem device.

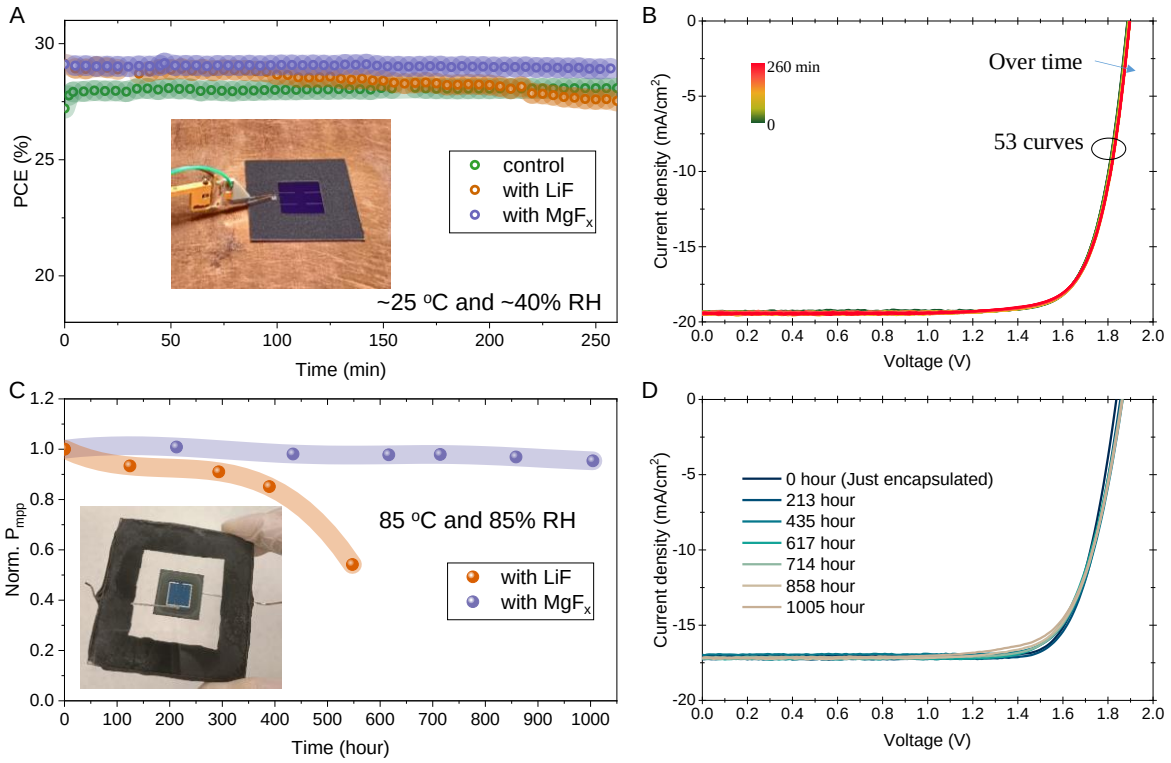

Fig. 4. Stability tests. (A) Evolution of the photovoltaic performance under continual AM 1.5G illumination for over 4 hours in air. J-V scans were performed each ~5 min. The inset is the photo of one device under test with a black aperture mask on it. (B) J-V curves of the tandem devices with MgF_x interlayer under continual AM 1.5G illumination. (C) Photovoltaic-performance evolution of the encapsulated tandem devices, when subjected to a damp-heat stability experiment at 85 °C and 85% RH. The inset is the photo of one encapsulated device. (D) J-V curves of the tandem devices during damp heat tests.

Submitted Manuscript: Confidential
Template revised February 2021

Supplementary Materials for

Efficient and stable perovskite-silicon tandem solar cells through contact displacement by MgF_x

Jiang Liu[1]*, Michele De Bastiani[1], Erkan Aydin[1], George T. Harrison[1], Yajun Gao[1], Rakesh R. Pradhan[1], Mathan K. Eswaran[1], Mukunda Mandal[2], Wenbo Yan[1], Akmaral Seitkhan[1], Maxime Babics[1], Anand S. Subbiah[1], Esma Ugur[1], Fuzong Xu[1], Lujia Xu[1], Mingcong Wang[1], Atteq ur Rehman,[1] Arsalan Razzaq[1], Jingxuan Kang[1], Randi Azmi[1], Ahmed Ali Said[1], Furkan H. Isikgor[1], Thomas G. Allen[1], Denis Andrienko[2], Udo Schwingenschlögl[1], Frédéric Laquai[1], Stefaan De Wolf[1]*

[1]King Abdullah University of Science and Technology (KAUST), KAUST Solar Center (KSC), Physical Sciences and Engineering Division (PSE); Thuwal 23955-6900, Kingdom of Saudi Arabia
[2]Max Planck Institute for Polymer Research, 55128 Mainz, Germany

*Corresponding author. Email: jiang.liu@kaust.edu.sa; stefaan.dewolf@kaust.edu.sa

This PDF file includes:

Materials and Methods

Materials

Patterned tin-doped indium oxide (ITO) (~15 Ω/sq) coated glass was purchased from Xin Yan Technology LTD. Lead iodide (PbI_2, 99.999%) and lead bromide ($PbBr_2$, 99.999%) were purchased from Alfa Aesar. Formamidinium iodide (FAI), methylammonium bromide (MABr) were purchased from Greatcell Solar. Cesium iodide (CsI, 99.999%), anhydrous dimethylformamide (DMF, anhydrous, 99.8%), anhydrous dimethyl sulfoxide (DMSO, anhydrous, ≥99.9%), anhydrous chlorobenzene (CB, anhydrous, 99.8%), lithium fluoride (LiF) were purchased from Sigma-Aldrich. Sodium fluoride (NaF) and magnesium fluoride (MgF_x) were purchased from Plasmaterials, Inc. [2-(9H-carbazol-9-yl)ethyl]phosphonic acid (2PACz) was purchased from TCI. C_{60} (>99.5% purity) was purchased from Nano-C. Bathocuproine (BCP, >99.5% purity) was bought from Ossila Ltd. The ceramic 2-inch IZO target was purchased from Plasmaterials, Inc. All the chemicals were used as received without further purification.

Si bottom cell fabrication

4-inch *n*-doped float-zone (FZ) Si wafer with a thickness of 260-280 μm was used for Si bottom cell fabrication. The double-side texture structure with random distributed pyramids was obtained using an alkaline solution. The size of the pyramids is controlled by adjusting the alkaline concentration and the process temperature. The wafers were dipped in hydrofluoric acid solution followed by cleaning process, before transferred into a plasma enhanced chemical vapour deposition (PECVD) cluster (Indeotec Octopus II) for amorphous silicon (a-Si) deposition. 8 nm intrinsic (i), 6 nm n-doped, and 13 nm p-doped a-Si layer were grown on wafer using the PECVD cluster tool. The process temperatures are 200 °C. 150 nm ITO and 250 nm Ag were sputtered on the backside of the wafer through a shadow mask of 1.1 x 1.1 cm^2. 15 nm IZO recombination junction was sputtered on the front side through an aligned mask with an opening area of 1.1 x 1.1 cm^2. In order to recover sputtering damage, an annealing step at 200 °C for 10 min was carried out. The wafer was then laser-cut to 2.2 cm x 2.2 cm square substrate for tandem fabrication.

Perovskite top cell fabrication on Si bottom cell

The Si bottom wafers were subjected to UV-Ozone treatment for 10 min before transferred into the glovebox. For 2PACz deposition, 1 mg/mL 2PACz in ethanol was used. The 2PACz as hole transport layer (HTL) was spin-coated on ITO-coated substrates at 5000 rpm for 30 s, followed by drying at 100 °C for 10 min. 1.7 M $Cs_{0.05}FA_{0.8}MA_{0.15}Pb(I_{0.755}Br_{0.255})_3$ perovskite precursor solution was prepared by dissolving a mixture of FAI, MABr, CsI, PbI_2, and $PbBr_2$ in a mixed solvent of DMF and DMSO with a volume ratio of 4:1. The perovskite films were spin-coated at 2000 rpm for 45 s an acceleration of 400 rpm/s, then followed with 7000 rpm for 10 s with an acceleration of 5000 rpm/s. Chlorobenzene of 200 μL was dropped in the center of the substrates 12 s before the end of the spin-coating process. After the rotation ceased, the substrates were immediately transferred onto a hotplate of 100 °C and were annealed for 15 min. After perovskite deposition, ~1 nm metal fluorides (NaF, LiF, MgFx or CaFx) were deposited by thermal evaporation. The samples were then quickly transferred to a C_{60} evaporation chamber to minimize air exposure as much as possible. During the transfer process, the samples may be exposed to air for a short period of time, but we did not find that this process obviously affected the device performance. 15 nm C_{60} were subsequently deposited by thermal evaporation. 20 nm SnO_2 was then deposited by atomic layer deposition (ALD) using a Picosun system. The substrate temperature was maintained at 100 °C during ALD deposition with TDMASn precursor source at 80 °C and H_2O source at 18

°C. The pulse and purge time for Tetrakis(dimethylamino)tin(IV) (TDMASn) is 1.6 and 5.0 s with a 90 sccm carrier gas of nitrogen, for H_2O is 1.0 and 5.0 s with 90 sccm N_2. 140 cycles was used. 70 nm IZO was sputtered from a 3-inch IZO ceramic target on top of the SnO_2 through a shadow mask. Ag finger with a thickness of 500 nm was thermally evaporated using a high precision shadow mask. Finally, 100 nm MgF_x was thermally evaporated as an anti-reflection layer. The thickness of C_{60}, IZO and metal fluoride layers were first calibrated by spectroscopic ellipsometry. The evaporation rate and thickness of each experiment were monitored by quartz crystal microbalance sensors.

Single-junction perovskite solar cell fabrication

ITO glasses were ultrasonically cleaned with detergent, deionized water, acetone, and isopropanol successively, and then blow-dried with compressed nitrogen. The substrates were subjected to UV-Ozone treatment for 10 min before any film deposition. The processes for HTL and perovskite are the same as that on tandem devices. After perovskite deposition, fluoride-based interlayer, 25 nm C_{60}, 5 nm BCP and 100 nm Ag layers were thermally evaporated on perovskite films sequentially.

Device encapsulation and stability tests

The tandem device was sandwiched between two 3-mm-thick cover glass/encapsulant with black butyl rubber sealant at the edges. The device was vacuum-laminated in an industrial laminator (Ecolam5 Ecoprogetti) at 120°C for 20 min. Tinned plated copper strips were used to contact the upper and lower electrodes of the tandem devices using Ag paste, and were extended to the outside of the cover glass. For damp heat test, the devices were placed inside an environmental chamber with a condition of 85 °C and 85% relative humidity, and were taken out for J-V measurement at some intervals.

Solar cell Characterization

Single-junction opaque devices were tested in a glove box using Keithley 2400 at room temperature under AM 1.5G illuminations (1000 W/m^2) from an Abet Technologies Sun 3000 solar simulator which was calibrated using a standard silicon cell (RERA). Current-voltage (J-V) curves were obtained both in reverse (1.3 V → -0.1 V) and forward scan (-0.1 V → 1.3 V) with a step size of 10 mV. J-V measurements on tandem devices were performed in the air under LED-based solar simulator (WaveLabs Sinus 220). About 200 mV/s scan speed was used and no preconditioning was used in this work. A mask with an aperture area of 1.0 cm^2 for tandem device was used. The light intensity was calibrated using Fraunhofer ISE CalLab certified c-Si solar cells.

UPS/LE-IPES/XPS

The electron spectroscopy measurements of ultraviolet photoelectron spectroscopy (UPS), X-ray photoelectron spectroscopy (XPS) and low energy inverse photoemission spectroscopy (LE-IPES) were conducted in a single UHV ScientaOmicron system at 10^{-9} mbar. The surface work function and valence region were studied by UPS with a vacuum ultraviolet unfiltered He(1) (21.22 eV) source (focus), with an aperture attenuation. The samples was biased to -10 V to observe the secondary electron cut-off. To obtain a spectra of He(1) α, the satellite He(1) β 1.87% (23.09 eV) and α 0.35% (23.74 eV) components were subtracted, by first measuring the fermi step edge step of a clean (Argon sputtered) Au film. Repeated scans were recorded to assess any shifts resulting from photoemission induced surface charging. A constant pass energy of 5 eV was used and E_F reference made to the measured Au film. The photoelectrons were measured with hemispherical

analyzer Sphera II EAC 125 analyzer and 7 channeltron detector positioned normal to the sample. For each UPS measurement, it takes 50-100 s time with a fluence of ~2×10^8 photons/mm^2/s and a spot diameter of ~3 mm. The work function was determined by intersection of a linear extrapolation to the baseline. For all the perovskite and perovskite/interlayer samples, the band edge was determined by fitting the spectral edge using Gaussian function and then subtracting the Gaussian peak position by 2.9σ (*39*). For the C_{60}-coated samples, the band edge was determined by subtracting the Gaussian peak position by 2.0σ (*40*).
The LE-IPES was conducted in a homemade system in the Bremsstrahlung isochromatic mode in the adjoining chamber consisting of a monoenergetic electron source (Staib) of 0.25 eV energy dispersion and drain current of 20-40 μA with a 2-3 mm sized electron spot, directed normal to the sample surface. The emitted IPES light was detected through a lens assembly (vacuum and airside), bandpass filter of 280 nm (4.43 eV), and solid-state photo-multiplier tube (PMT) (Hamamatsu). Vacuum level calibration was made to the turn-on point in the drain current energy trace recorded simultaneously with the PMT signal, accounting for the band pass energy. A similar methodology to the UPS spectra was adopted to determine the CBM, fitting a Gaussian function and assigning the position as 2.9sigma. Plots of UPS and IPES are constructed taking into account the shared E_F position and arbitrarily adjusted in intensity.
Note that all the samples for this surface-sensitive analysis was loaded in a glovebox, and were transferred into the UHV system using a closed transfer box to minimize air exposure as much as possible. The UPS UHV system is equipped with one small thermal evaporator where C_{60} depositions were conducted. The thickness of evaporated C_{60} layer was monitored by a quartz crystal microbalance. For the measurements of the samples with different C_{60} thickness, the samples were transferred back and forth several times between the C_{60} evaporation chamber and analysis chamber without breaking the vacuum.
XPS was conducted with a monochromated Al Kα 1487.6 X-ray source, with the samples in electrical contact to the analyzer at ground potential. The photoelectrons were also measured from the same spot as used for UPS and directed normal to the surface plane to the analyzer (same as analyzer as used in UPS). A two point binding energy calibration was made with the measurement of a clean Au films E_F step edge and Au 4f core level 84.1 eV. The X-ray source power is around 380 W with a 10 mm-sized spot. Quantification of XPS spectra were conducted in CASAXPS(r), integrating the peak areas using a Tougaard based background function and accounting for the instrumental transmission function, mean free path and Scofield RSFs of Mg1s (11.18), F1s (4.43) and O1s 2.93.

Kelvin probe force microscopy (KPFM) measurement
KPFM potential and topographic mappings were obtained using a Digital Instruments Multimode AFM (Veeco Metrology Group). AFM tips (model: OSCM-PT) with nominal spring constant 0.5-4. N/m and 20 nm PtTi coating was used. The perovskite films were deposited on 2PACz/ITO-coated Si substrate. The substrates were grounded and measurements were performed in air.

Transient-absorption spectroscopy (TAS)
Transient absorption measurements were performed using a commercial setup (Helios, Ultrafast Systems). The pump pulse has a wavelength of 600 nm. The reason to choose this relatively-longer wavelength is out of the consideration that it is close to the bandgap of perovskite films and hence the hot-carrier related effects can be neglected. The pump pulse comes from an optical parameter amplifier (TOPAS-C from Light Conversion) which is pumped by an 800-nm laser seed (~100 fs

pulse, 1 kHz, Astrella, Coherent). The probe light ranges a broad spectral region, from 450 to 1000 nm. This broad-band probe light is generated by pumping a 2-mm thick calcium fluoride crystal with an 800-nm pulse which also originates from the same seed laser amplifier (~100 fs pulse, 1 kHz, Astrella, Coherent). This fraction of 800-nm pulse passes through a mechanical delay line before reaching the sample, so as to obtain precisely-manipulated delay time in reference to the 600-nm pump pulse. Moreover, to improve the data acquisition process a small fraction of the probe light is also acquired. Throughout the whole measurement process, we also closely monitor the possible degradation of perovskite films by comparing the acquired results from each specific scan. We did not observe any degradation during the measurement. All the samples were measured at room temperature and ambient conditions. The laser excitation fluence varies from 38 to 159 uJ/cm^2.

One-dimension carrier diffusion/recombination model was used to fit the decay curves. This model has been successfully used in both inorganic semiconductors (*41*) and perovskites (*42*) as well. It is briefly introduced as follows.

$$\frac{\partial N(x,t)}{\partial t} = D\frac{\partial^2 N(x,t)}{\partial x^2} - (k_1 N(x,t) + k_2 N(x,t)^2 + k_3 N(x,t)^3) \quad (1)$$

Initial carrier distribution: $N(x,0) = N(0,0) \times \exp(-\alpha\, x)$ (2)

Boundary conditions (front and back interface recombination velocities):

$$\left.\frac{\partial N(x,t)}{\partial x}\right|_{x=0} = \frac{S_f}{D} N(0,t) \quad (3)$$

$$\left.\frac{\partial N(x,t)}{\partial x}\right|_{x=d} = -\frac{S_b}{D} N(d,t) \quad (4)$$

Herein, N(x, t) denotes to carrier density which is a function of both space (x) and time (t); S_f and S_b denote surface/interface recombination velocities at the front (f) and back (b) surfaces/interfaces, respectively; bulk-specific parameters are the diffusion coefficient (D) and the 1st (k_1), 2nd (k_2), and 3rd (k_3) order recombination coefficients; α is the absorption coefficient; d represents the film thickness. The unique feature of this model is that it not just takes into account bulk recombination (k_1, k_2, k_3) and diffusion, but also takes into account what is happening on the surface/interface.

The global fitting is done in such a way. All bulk related parameters (D, μ, k_1, k_2, k_3) are shared for all of these three samples, since they all have the same active layer (please refer to the sample structure). Meanwhile, the S_f parameter varies between different samples. Following such a procedure, we could improve the fitting accuracy and extract exclusively information of the surface.

Transmission electron microscope (TEM) analysis

The EDX mapping of the cross-sectional tandem cells were investigated in Titan Cs Probe TEM equipped with EDX and HAADF detector in STEM mode at 300 kV operating voltage. The cross-sectional lamella was prepared first in a scanning electron microscope (Helios G4 DualBeam, FEI), equipped with an EasyLift nanomanipulator with the help of a Ga focused ion beam (FIB). To

protect the sample, the protective carbon and platinum layers were deposited under electron and ion beams.

Photoluminescence measurement

Steady photoluminescence (PL) and time-resolved photoluminescence (TRPL) measurements were carried out with a spectrofluorometer (Fluoroma-Modular, Horiba Scientific). For steady PL, 500 nm monochromatic light was continuously illuminated on the surface of the films. Emission spectra with wavelengths between 650 nm and 850 nm were collected. For TRPL, a 633 nm pulsed laser which was generated from a picosecond laser diode (PicoQuant) was used for the pump excitation. The fluence is estimated to be around ~10 nJ/cm^2. A long-pass 650 nm filter was used, and 738 nm light was probed.

For QFLS mapping, the perovskite films on 2PACz/ITO coated Si cell were encapsulated in a nitrogen glovebox using an ultra-thin glass cover slide with edge sealed by UV-curable epoxy. The absolute PL spectra was obtained using hyperspectral luminescence imaging system equipped with an optical microscope with a 20 X objective and a 532 nm laser with controlled laser intensity. The integration of photon numbers over the photon energy was obtained using Matlab, and was then used to calculate J_{rad}. The quasi-Fermi level splitting (*QFLS*) was obtained following the equation kT*ln($J_{rad}/J_{o,rad}$). To reduce the noise, 5X5 data binning was adopted.

Electroluminescence measurement

The electroluminescence (EL) spectra was recorded using hyperspectral luminescence imaging system equipped with an optical microscope with a 20 X objective. Bare tandem devices without encapsulation were used. Keithley 2401 source meter was used as current source to drive our tandem device, and a home-made matlab-based program is used to record voltage and current data as function of time. The injection current varies from 10 μA /cm^2 to 30 mA/cm^2. It takes almost 6 minutes for each injection current J_{inj}. Photometric calibration was conducted to convert the spectra to a calibrated spectral photon flux defined as number of photons arriving at the pixel per unit of time, per unit of photon energy (in eV), per unit surface.

Pseudo JV Reconstruction

The pseudo JV of perovskite subcells in the tandem was obtained based on injection current-dependent EL measurements, while for silicon subcell, Suns-V_{OC} method, in which the V_{OC} values of one Si single-junction cell were recorded under different illumination intensity, was employed. The pseudo JV curves of each subcell are shifted to the J_{sc} (based from EQE cruves) points of the corresponding sub-cells. Then the pseudo JV curves of the two sub-cells are numerically summed to obtain the final pseudo JV curves.

Following previously established processes (*43*), the approach explained below is used to calculate quantum efficiency of electroluminescence (EQE_{EL}) and extract the quasi-Fermi level splitting ($QFLS_{EL}$) of perovskite subcells.

EQE_{EL} is define as the ratio of radiative recombination current (J_{rad}) to injection current (J_{inj}). $QFLS_{EL}$ could be calculated using

$$QFLS_{EL} = kT * \ln\left(\frac{J_{rad}}{J_{0,rad}}\right) = kT * \ln(EQE_{EL} * \frac{J_{inj}}{J_{0,rad}})$$

Assuming that the device is at 300 K in thermal equilibrium with its environment, the dark radiative recombination current is

$$J_{0,rad} = \mathrm{q}\int_0^\infty EQE(E) * \Phi_{BB}(E)dE$$

where $EQE(E)$ is quantum efficiency of perovskite subcell in the tandem. $\Phi_{BB}(E)$ in unit of photons/(m^2.s.eV) is the black-body radiation of the surroundings at 300K, and is defined as

$$\Phi_{BB}(E) = \frac{2\pi E^2}{h^3c^2}\frac{1}{\exp(\frac{E}{kT}) - 1}$$

with h plank's constant, k Boltzmann constant and T temperature.
$J_{o,rad}$ could be calculated by integrating the product of the external quantum efficiency (EQE) and the black body spectrum Φ_{BB} at 300 K over the energy, as shown in Fig. S23.

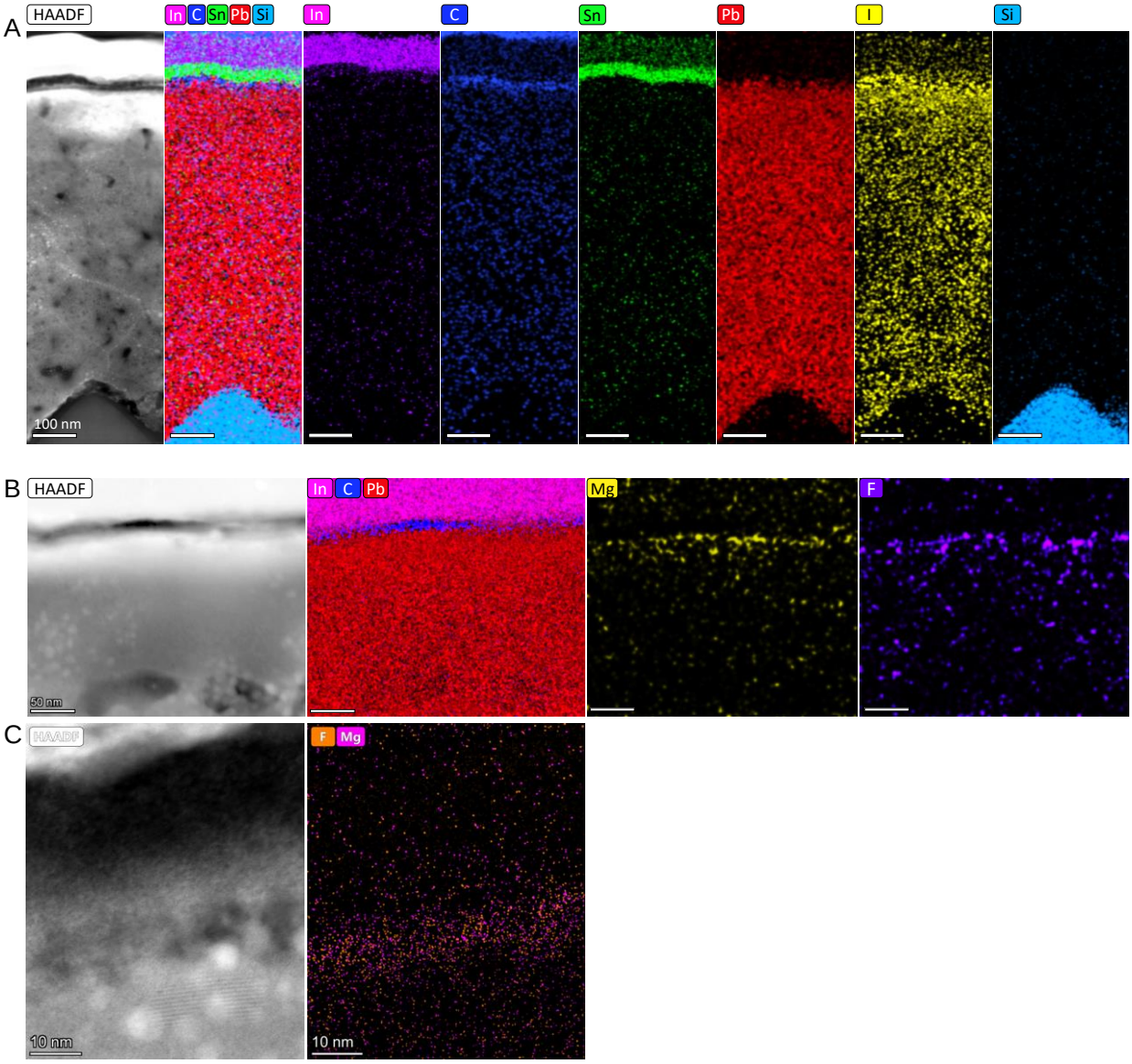

Fig. S1. High-resolution cross-sectional TEM images and the EDX mapping of perovskite/Si tandem. (A) The completed perovskite subcell on textured Si. (B) The perovskite/MgF_x/C_{60}/SnO_2 interface position. (C) Another location for the perovskite/MgF_x/C_{60}/SnO_2 interface.

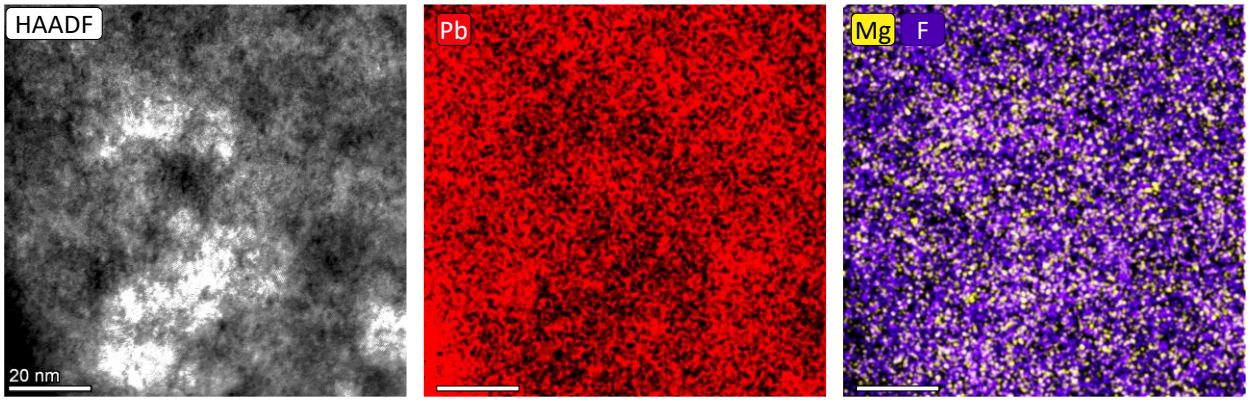

Fig. S2. Top-view TEM images and EDX mapping of perovskite/MgF_x sample. In this top-view specimen, the perovskite and MgF_x layer were successively deposited on a TEM grid.

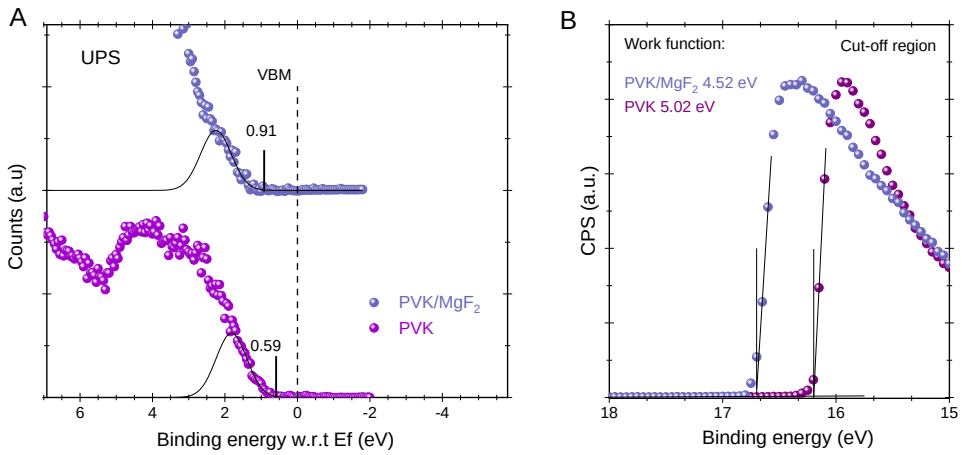

Fig. S3. UPS results of the second perovskite and perovskite/MgF_x samples. (A) Valence photoemission spectra. (B) Secondary electron cut-off (SECO) region.

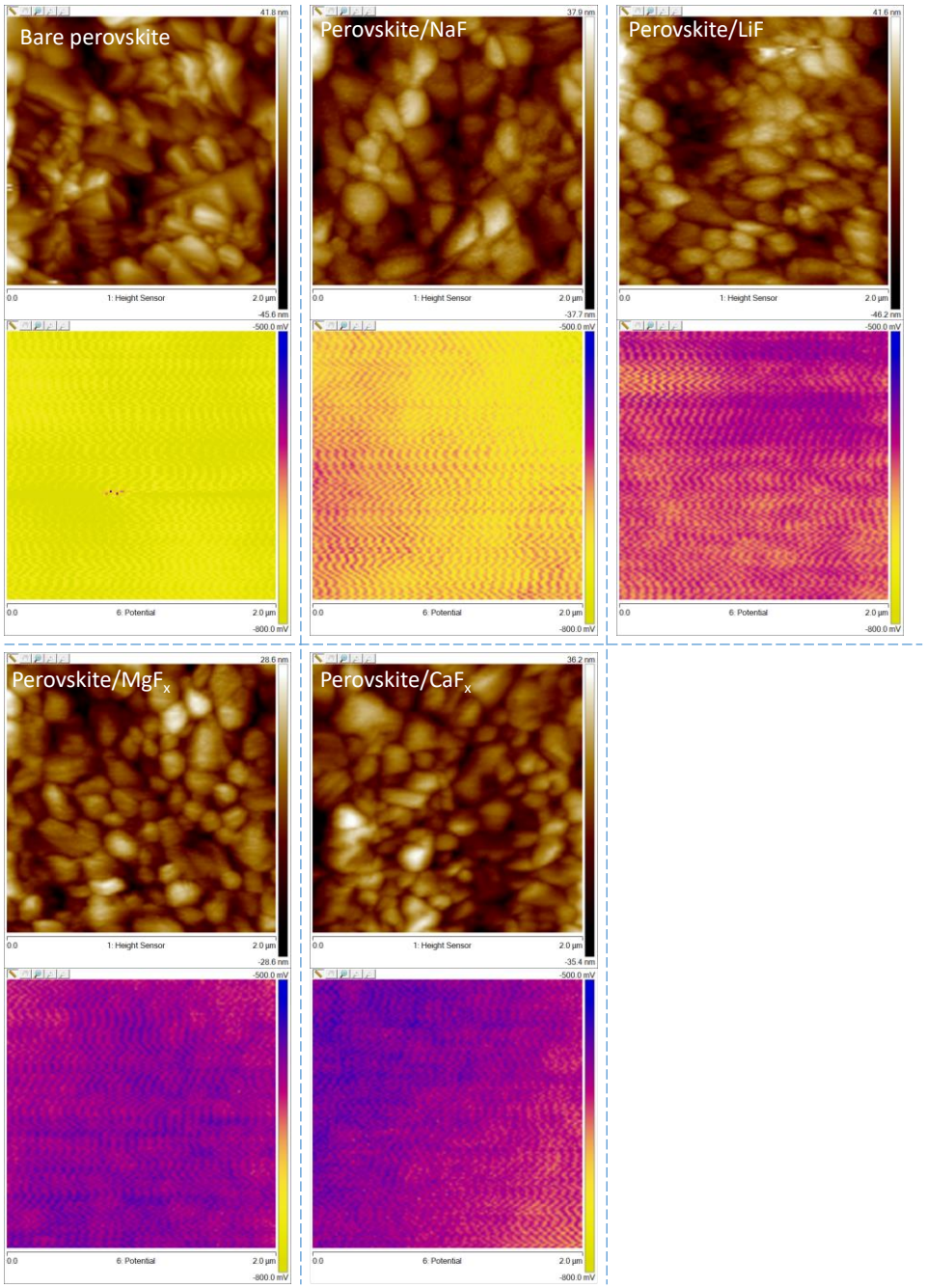

Fig. S4. AFM height and the corresponding KPFM surface potential maps for the perovskite film and those perovskite films coated with metal fluoride layer.

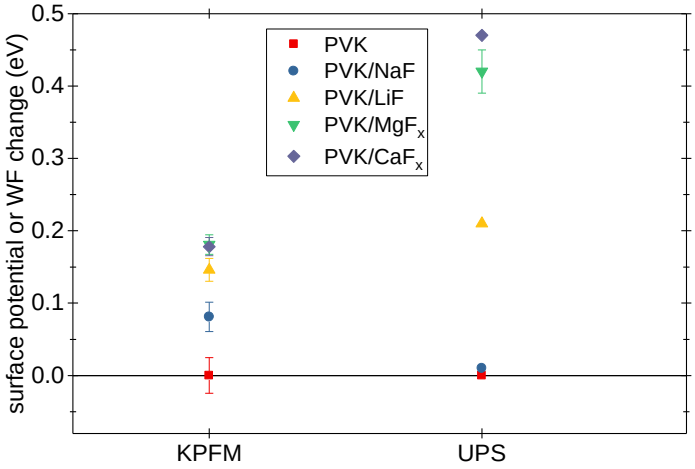

Fig. S5. Comparison of the WF change of the perovskite films coated with interlayers using KPFM and UPS techniques.

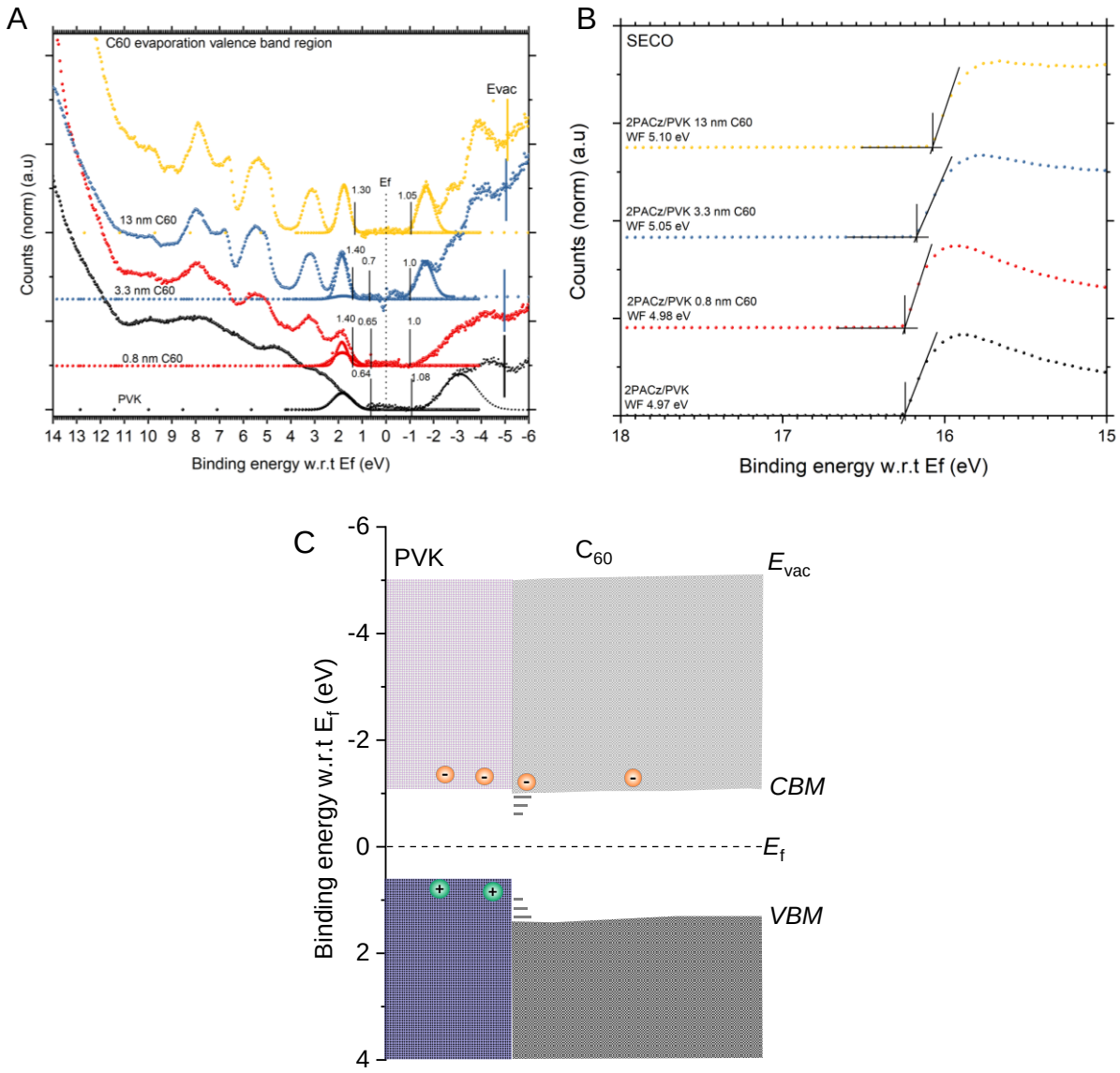

Fig. S6. UPS and LE-IPES results of perovskite/C_{60} sample with different thickness of C_{60} layer. (A) Valence photoemission spectra and IPES spectra of the perovskite and the samples coated with different thicknesses of the C_{60} layer. From IPES, the CBM position relative to E_F can be extracted. All energies are referenced to a common Fermi level (0 eV). (B) Secondary electron cut-off (SECO) region. (C) Experimentally determined energy level diagrams of the ETL-side interface without any interlayer.

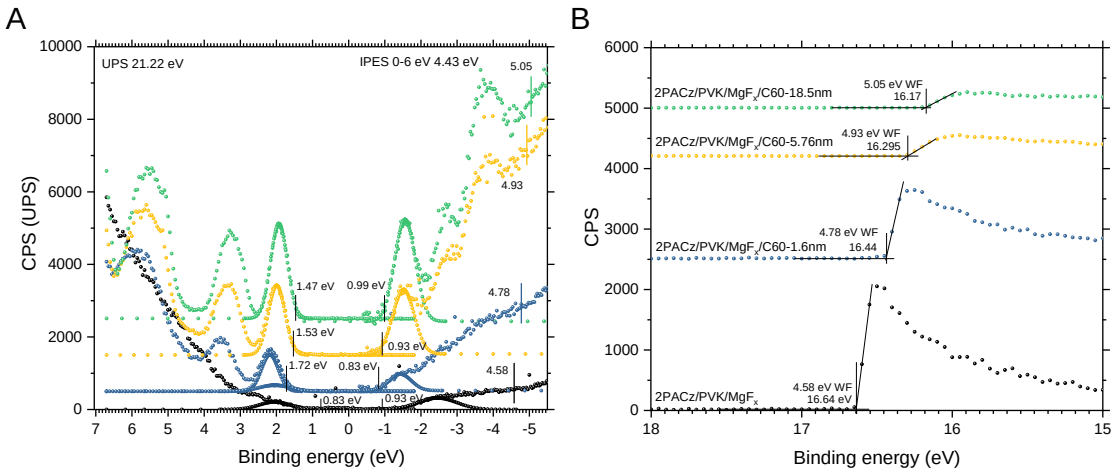

Fig. S7. UPS and LE-IPES results of perovskite/MgF_x/C_{60} sample with different thickness of C_{60} layer. (A) Valence photoemission spectra and IPES spectra of the perovskite samples as a function of C_{60} thickness. (B) Secondary electron cut-off (SECO) region.

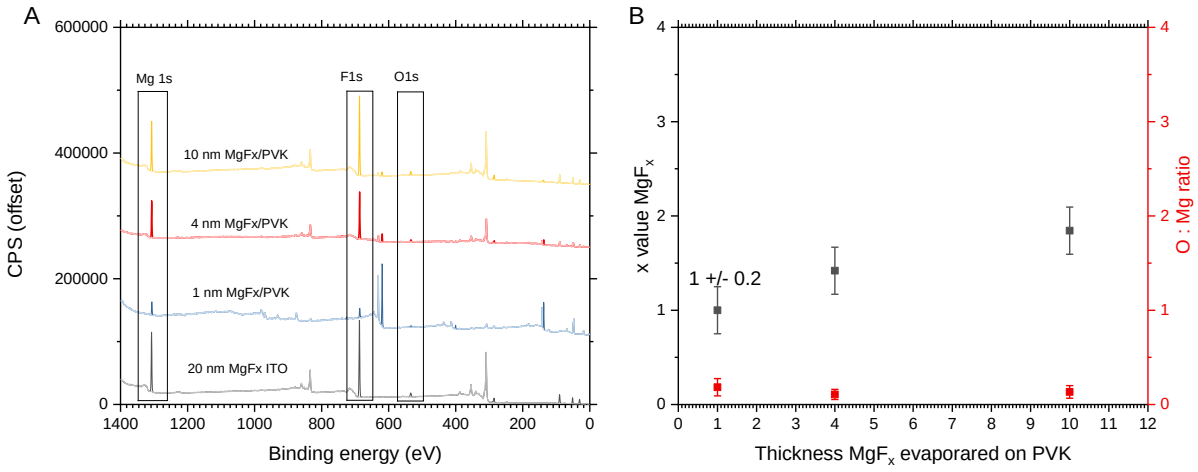

Fig. S8. XPS composition analysis of evaporated MgF_x films. (A) XPS survey spectrum. (B) Elemental composition ratio.

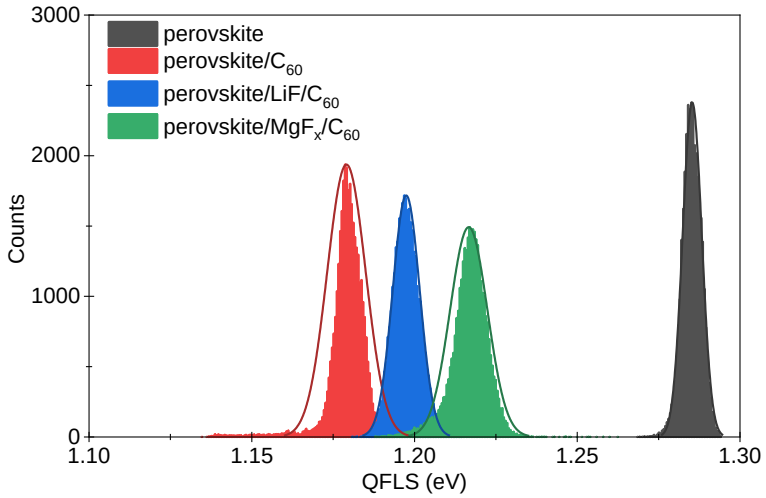

Fig. S9. Histogram of QFLS mapping for the perovskite, perovskite/C_{60}, perovskite/LiF/C_{60}, and perovskite/MgF_x/C_{60} samples

Table S1. Extracted TRPL lifetime of Figure. Bi-exponential fitting method with the equation $A(t)=A_1\exp(-t/\tau_1)+A_2\exp(-t/\tau_2)+B$ was used. Average PL decay time τ_{ave} is calculated using the equation $\tau_{ave}= (A_1\tau_1+A_2\tau_2)/(A_1+ A_2)$.

Samples	bi-exponential fitting				
	τ_1 (ns)	A_1 %	τ_2 (ns)	A_2 %	τ_{ave} (ns)
perovskite	809	50.7%	2501	49.3%	1643
perovskite/C_{60}	13	83.1%	92	16.9%	26
perovskite/LiF/C_{60}	12	70.1%	99	29.9%	38
perovskite/MgF_x/C_{60}	35	68.8%	189	31.2%	83

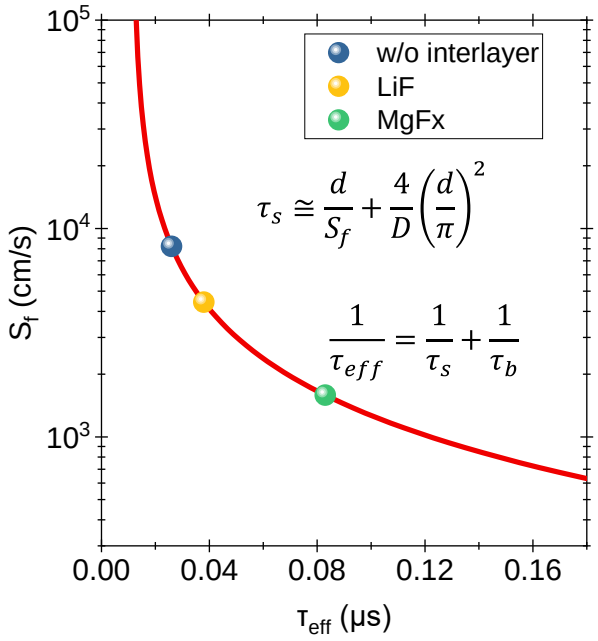

Fig. S10. Relation of the effective decay lifetime (τ_{eff}) and surface recombination velocity S_f. Assuming the S_b at 2PACz/perovskite interface is negligible and only the front interface S_f is considered, thus the surface lifetime τ_s is expressed as $\tau_s \cong \frac{d}{S_f} + \frac{4}{D}\left(\frac{d}{\pi}\right)^2$. The diffusion constant D= 0.49 cm^2/s were used. According to the equation $\frac{1}{\tau_{eff}} = \frac{1}{\tau_s} + \frac{1}{\tau_b}$, we can estimate the S_f for the perovskite/C_{60}, perovskite/LiF and perovskite/MgF_x cases, which are about 8.2×10^3, 4.4×10^3, 1.6×10^3 cm/s.

A

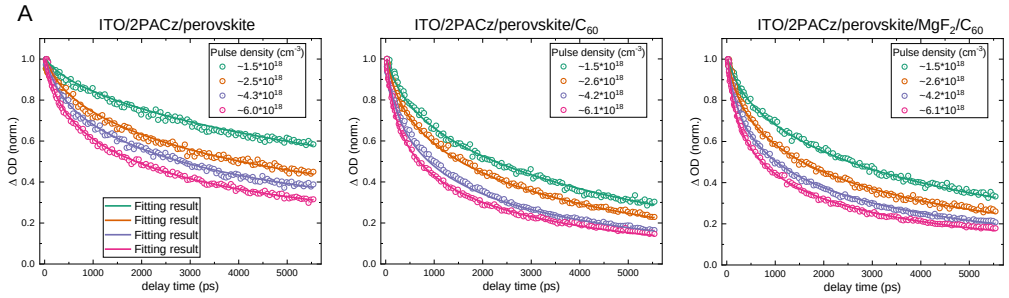

B

	Adj. R-square	D (cm^2s^{-1})	μ ($cm^2V^{-1}s^{-1}$)	D_L (nm)	k1 (s^{-1})	k2 ($cm^{-3}s^{-1}$)	k3 ($cm^6\ s^{-1}$)
Fitting results	0.99621	0.49±0.02	19.11±0.78	(1.19±0.07)×10^4	(3.48±0.3)×10^5	(1.04±0.4)×10^-10	(2.05±0.15)×10^-28

C

Samples	perovskite	perovskite/C_{60}	perovskite/MgF_2/C_{60}
S_f ($cm{\cdot}s^{-1}$)	0.25 ± 0.88	19338 ± 983	7598 ± 308

D

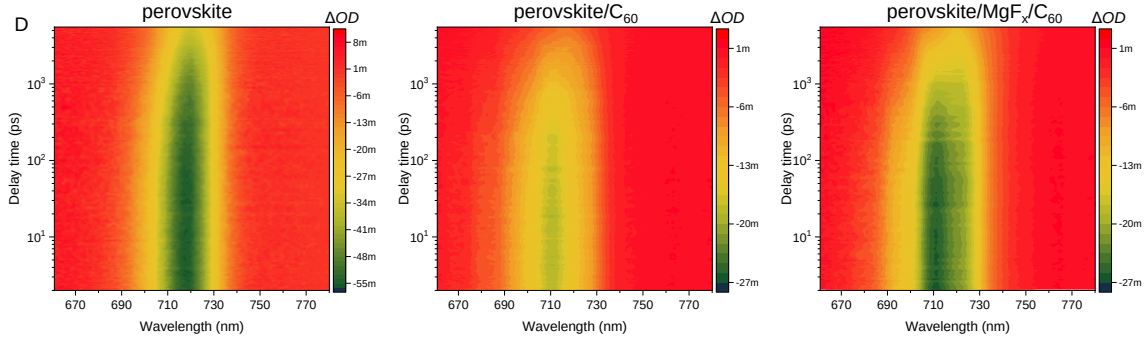

Fig. S11. TAS analysis of perovskite samples. (A) power-dependent decay dynamics for perovskite, perovskite/C_{60}, and perovskite/MgF_x/C_{60}. (B, C) Global fitting results based on the 12 curves of (A). Please note that the global fitting is performed for all of these dynamics, i.e., twelve curves (three samples and each with four different laser excitation densities). But for clarity, the results are presented separately based on each sample. (D) TAS of the perovskite samples under the laser pulse intensity of around 6×10^{18} cm^{-3}.

Supplementary text: DFT calculations

We conducted DFT calculation using a wide-bandgap mixed-cation mixed-halide perovskite with compsoition $Cs_{0.13}MA_{0.13}FA_{0.74}Pb(I_{0.81}Br_{0.19})_3$ and its bandgap close to our experiment. The structure is adopted from Ref. (*44*). We used the generalized gradient approximation of Perdew, Burke, and Ernzerhof (*45*) (Vienna ab-initio simulation package (*46*), VASP). A plane-wave cutoff energy of 500 eV was employed. The Brillouin zone was sampled on a 2 × 2 × 1 k-mesh in the structural relaxation and on a 5 × 5 × 1 k-mesh to calculate the density of states (DOS). The structural relaxation was considered to be converged when the Hellmann-Feynman forces were below 0.01 eV/Å for all atoms. Considering various orientations of the C_{60} molecule on $Cs_{0.13}MA_{0.13}FA_{0.74}Pb(I_{0.81}Br_{0.20})_3$, the structure shown in Fig. 2C was obtained after relaxation. The energetically favorable contact distance turned out to be 1.94 Å. The DOS obtained for this distance is shown in Fig. 2C. Formation of deep trap states within the bandgap of $Cs_{0.13}MA_{0.13}FA_{0.74}Pb(I_{0.81}Br_{0.20})_3$ is observed. Shifting the C_{60} molecule closer to the perovskite (d = 0.94 Å) leads to enhancement of the trap states, while shifting it away from the perovskite (d = 2.94 Å) suppresses the trap states.

We also conducted DFT calculations based on cubic $FAPbI_3$ (FA = Formamidinium) structure (*47*). Slab models were constructed with 5 PbI_2 and 5 FAI layers along the c-axis, exposing the PbI_2-terminated surface at the top and FAI-terminated surface at the bottom, analogous to the study of ref. (*48*). Consecutive slabs in the *c*-direction were separated by a vacuum layer with a thickness of at least 15 Å to eliminate spurious interaction with periodic images. The four model structures considered for this study are shown in Fig. S12. Periodic calculations were performed using the plane wave DFT implementation in VASP. Van der Waals interactions were incorporated employing Grimme's D3 method (*49*). The spin-orbit coupling (SOC) was not included in our calculations given the large system size explored in this study, and the fact that the generalized gradient approximation (GGA) in the PBE functional form can provide a reasonable estimation of the structure and its electronic properties (*50, 51*). The valence-core interactions were described with the projector augmented wave method (*46, 52*). The valence electrons considered in the calculations for each atom type are: Li (3), Mg (8), Pb (14), F (7), I (7), O (6), C (4), H (1), N (5). A plane-wave energy cutoff of 650 eV was used in all calculations. Forces of each atom smaller than 0.01 eV/Å were used during geometry relaxation. The structural relaxation was done by sampling the Brillouin zone on a 3 × 3 × 1 k-mesh. To counterbalance the "finite-size errors" of the slab models, dipole corrections were taken into consideration in our calculations. Structure visualization and projected DOS plotting were performed by the VESTA (*53*) and Sumo (*54*) packages. VASPKIT (*55*) was used for plotting the planar avarage electrostatic potentials.

Fig. S13F shows that if a C_{60} molecule is directly on top of the perovskite, a shallow trap state, composed of Pb(*p*) and I(*p*)-orbitals, is formed (indicated with grey arrow), which is a potential non-radiative recombination center and will lead to attenuated device performance. Moreover, in the absence of an interlayer in between FAPI and C_{60}, Fig. S14D reveals that the C_{60} molecule will interact with the FAPI layer, leading to a broadened VBM/HOMO of C_{60}. The use of an interlayer eliminates this interaction and we again observe sharp DOS peaks due to C(*p*) of C_{60} (Fig. S14E-F).

The presence of a surface dipole at the metal-fluoride/C_{60} interface can increase the local work function and hinder efficient electron extraction (*56*). The z-component of the dipole moment (D_z) is calculated to be maximal for the FAPI/C_{60} system (7.24 Debye, Fig. S15B) and is significantly

reduced by the insertion of an interlayer, falling to 2.07 Debye for the $(LiF)_n$-inserted case and 1.45 Debye for the $(MgF_2)_n$-inserted case. This trend is consistent with the trend in the work functions measured experimentally, making the $(MgF_2)_n$-inserted case to have the highest efficiency.

At the interlayer/C_{60} contact, the strongly electronegative F-atoms in the interlayer draw electron density from the *C*-atoms of the C_{60} molecule, and thus induces positive charge on C_{60}, as estimated by Bader charge analysis in Fig. S16B and Fig. S16C. Evidently, the $(MgF_2)_n$ layer acts as a better electron sink than the $(LiF)_n$ layer, as judged by the Bader charges of -1.56*e* in the interlayer and +0.11*e* in C_{60} for the $(LiF)_n$ case, as compared to -2.12*e* in the interlayer and +0.13*e* in C_{60} for the $(MgF_2)_n$ case (Fig. S16). This facilitates efficient charge extraction from the perovskite, more so in the $(MgF_2)_n$ case than the $(LiF)_n$ case.

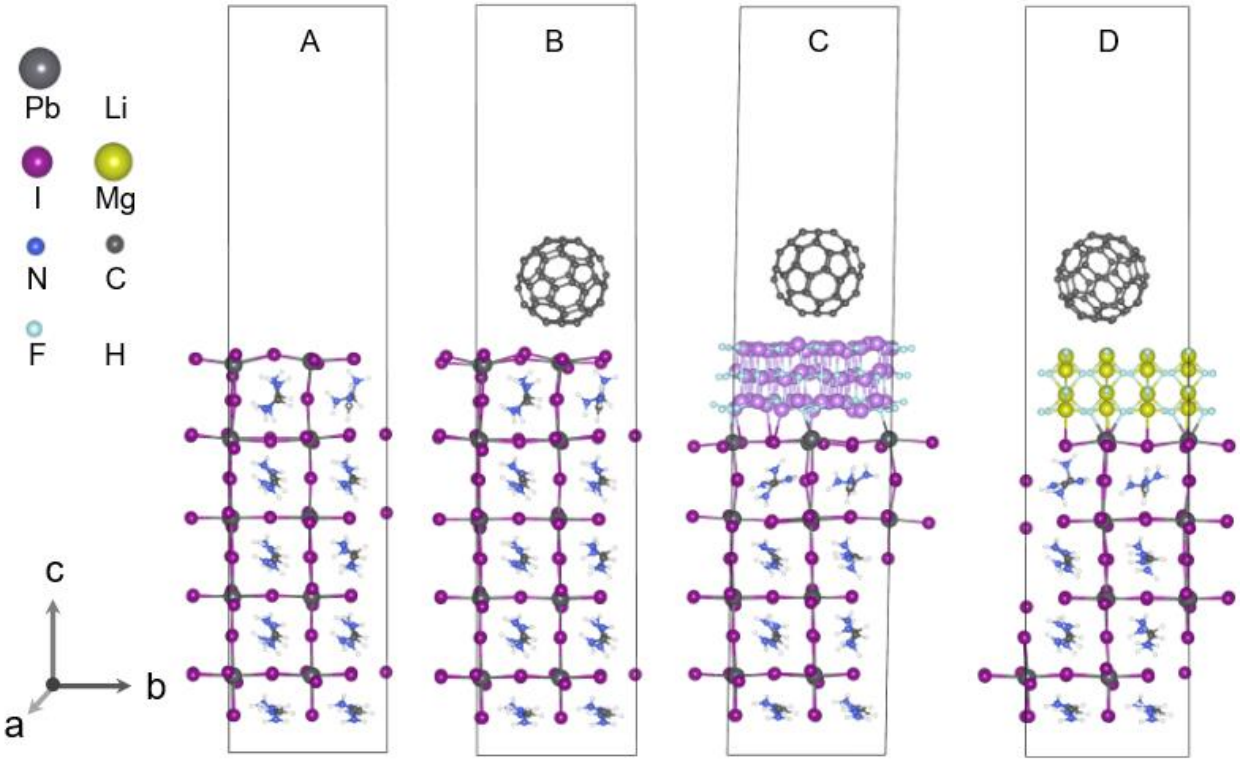

Fig. S12. Structures of four slab models considered in this study: **(A)** pristine FAPI, **(B)** C_{60} adsorbed over pristine FAPI layer, **(C)** $(LiF)_n$ interlayer in between FAPI and C_{60}, **(D)** $(MgF_2)_n$ interlayer in between FAPI and C_{60}.

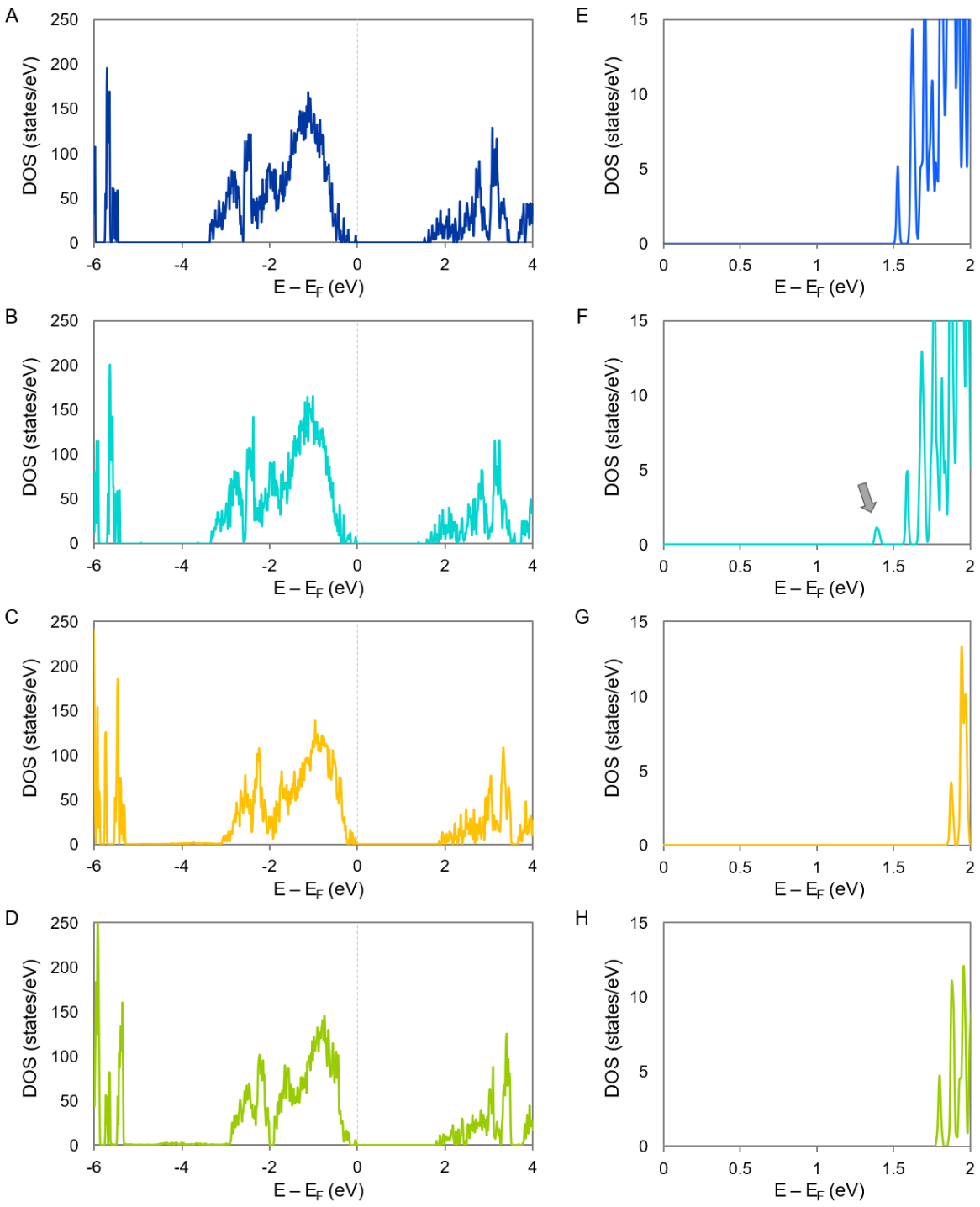

Fig. S13. Sum of projected densities of states of all atoms in the perovskite layer for: (A) pristine FAPI, (B) FAPI + C_{60}, (C) FAPI + $(LiF)_n$ + C_{60} and (D) FAPI + $(MgF_2)_n$ + C_{60}. The panels on the right (E-H) show the corresponding zoomed DOS between 0 to 2 eV.

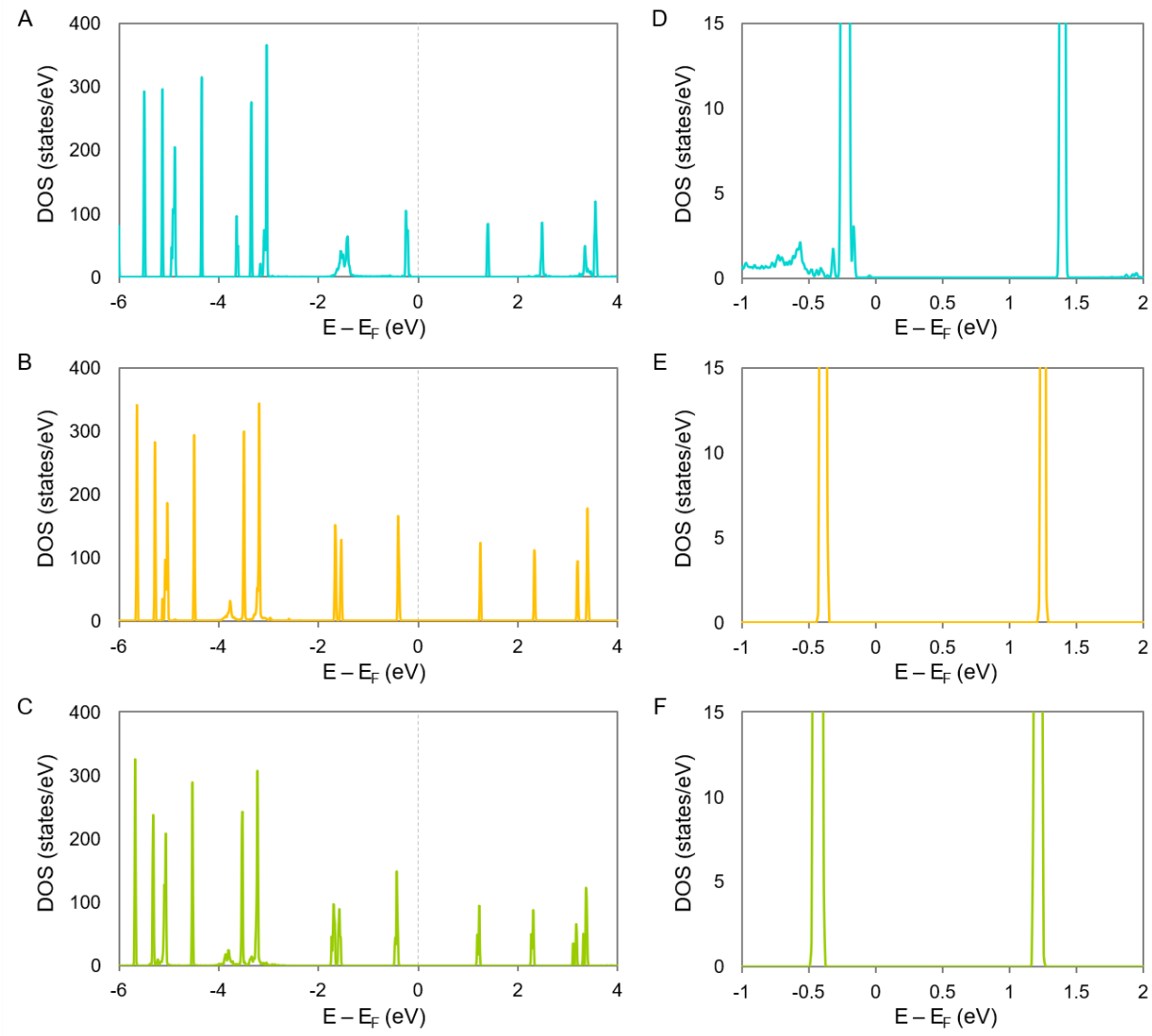

Fig. S14. Sum of projected densities of states of the C atoms constituting the C_{60} molecule in: (A) FAPI + C_{60}, (B) FAPI + $(LiF)_n$ + C_{60} (C) FAPI + $(MgF_2)_n$ + C_{60}. Panels on the right (D-F) shows corresponding zoomed in DOS at around 0 eV.

Planar-average electrostatic potential

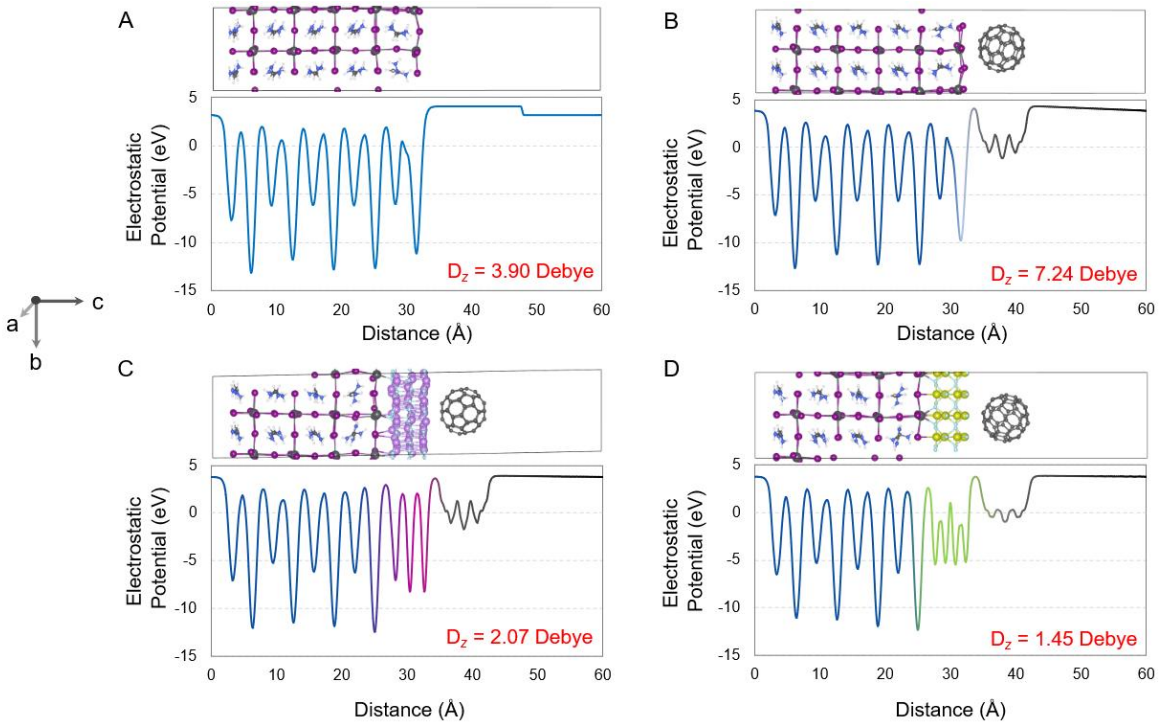

Fig. S15. Planar-averaged electrostatic potential as a function of distance (Å) from the bottom to the top vacuum layer shown for: (A) Pristine FAPI, (B) FAPI + C_{60}, (C) FAPI + $(LiF)_n$ + C_{60} and (D) FAPI + $(MgF_2)_n$ + C_{60}. The component of the dipole moment along the *c*-axis (D_z) is shown in each panel, which is the largest for C_{60} on top of FAPI (D_z = 7.24 Debye). The use of an interlayer significantly reduces D_z to 2.07 Debye for the $(LiF)_n$ case and 1.45 Debye for the $(MgF_2)_n$ case.

Plots of charge density difference and Bader charges

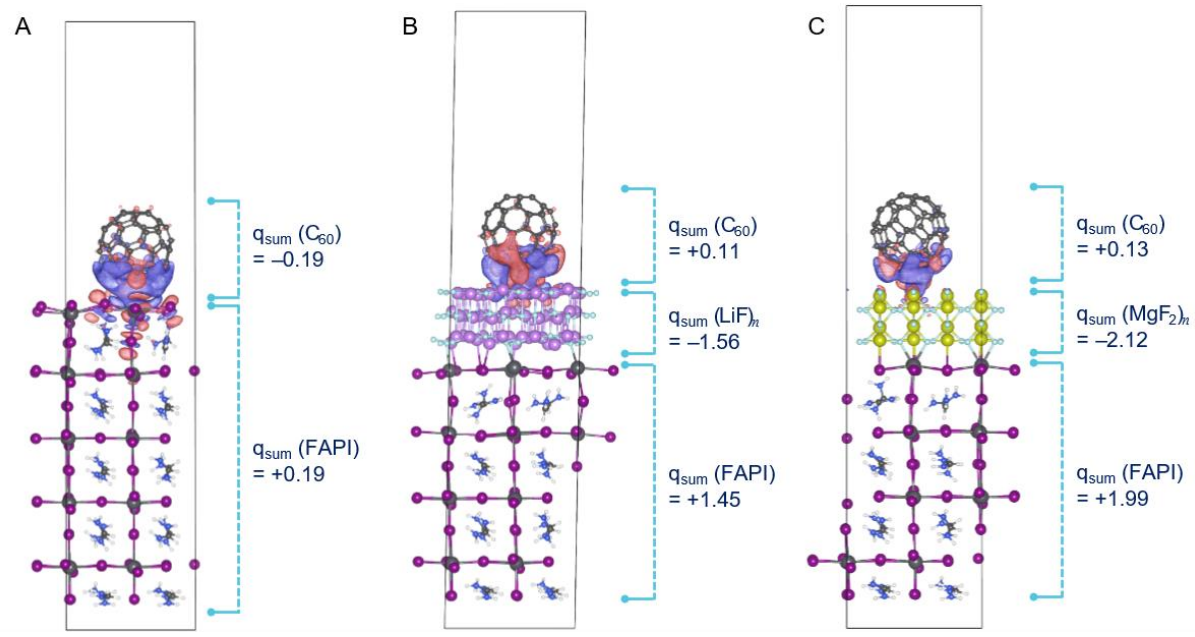

Fig. S16. Charge density difference plots (PBE) of three models involving C_{60}: (A) C_{60} on top of PbI_2-terminated FAPI, (B) C_{60} on top of FAPI/$(LiF)_n$ and (C) C_{60} on top of FAPI/$(MgF_2)_n$. (q_{sum} = sum of Bader atomic charges)

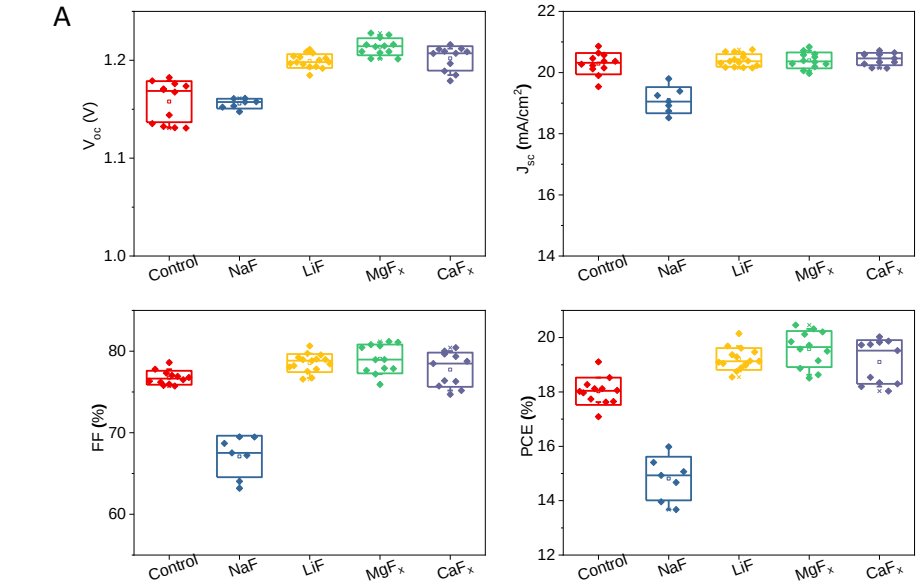

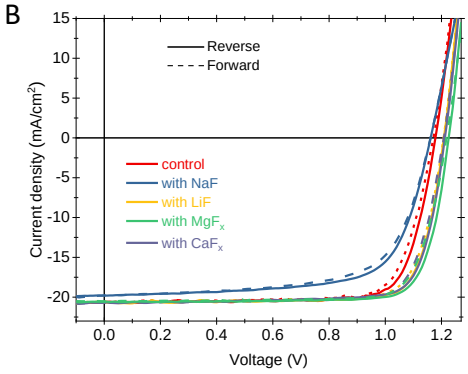

Devices	Scan conditions	V_{oc} (mV)	J_{sc} (mA/cm^2)	FF (%)	PCE (%)
control	FW	1172	20.59	77.6	18.73
	RV	1179	20.64	78.6	19.11
NaF	FW	1161	19.78	66.8	15.35
	RV	1161	19.80	69.5	15.98
LiF	FW	1207	20.60	78.8	19.61
	RV	1209	20.68	80.7	20.15
CaF_x	FW	1209	20.70	79.2	19.82
	RV	1212	20.65	80.0	20.03
MgF_x	FW	1218	20.51	79.4	19.82
	RV	1226	20.58	81.1	20.46

Fig. S17. Device performance of planar *p-i-n* PSCs without, and with metal fluoride interlayers. (A) Statistics of V_{oc}, J_{sc}, *FF*, and *PCE*. (B) *J-V* characteristics of the single-junction (SJ) perovskite devices.

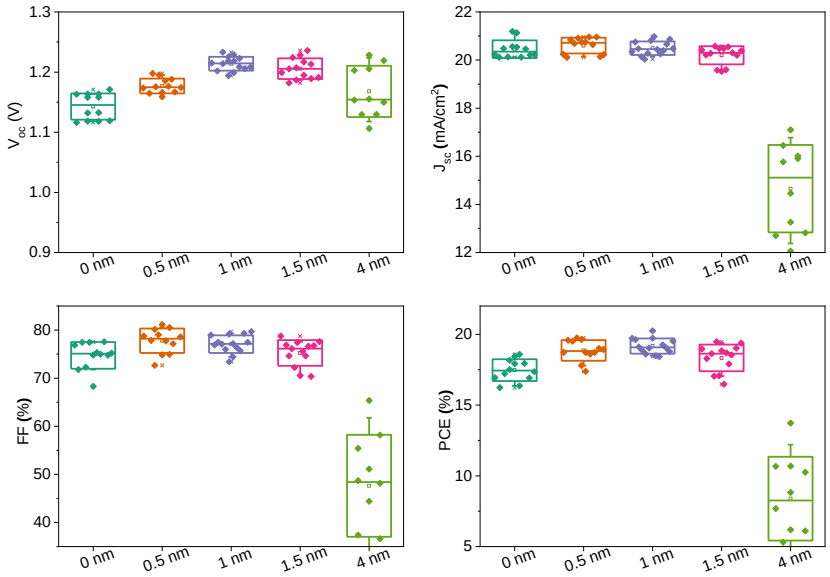

Fig. S18. Device performance of the single-junction perovskite devices with different MgF_x thickness.

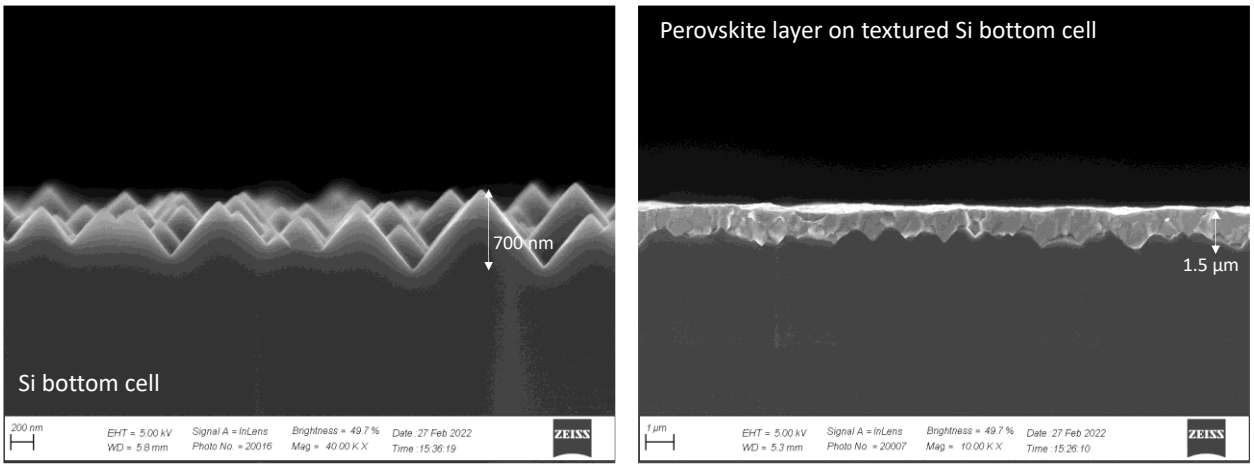

Fig. S19. Cross-sectional SEM images of our Si bottom cell and perovskite/silicon tandem.

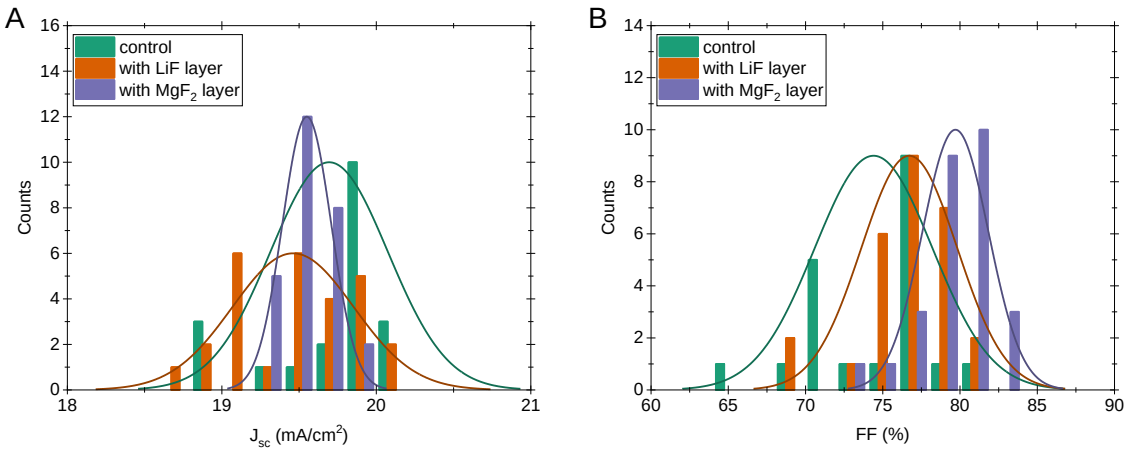

Fig. S20. Photovoltaic parameters (J_{sc} and *FF*) statistic of the tandem devices without an interlayer, and with LiF and MgF_x interlayer.

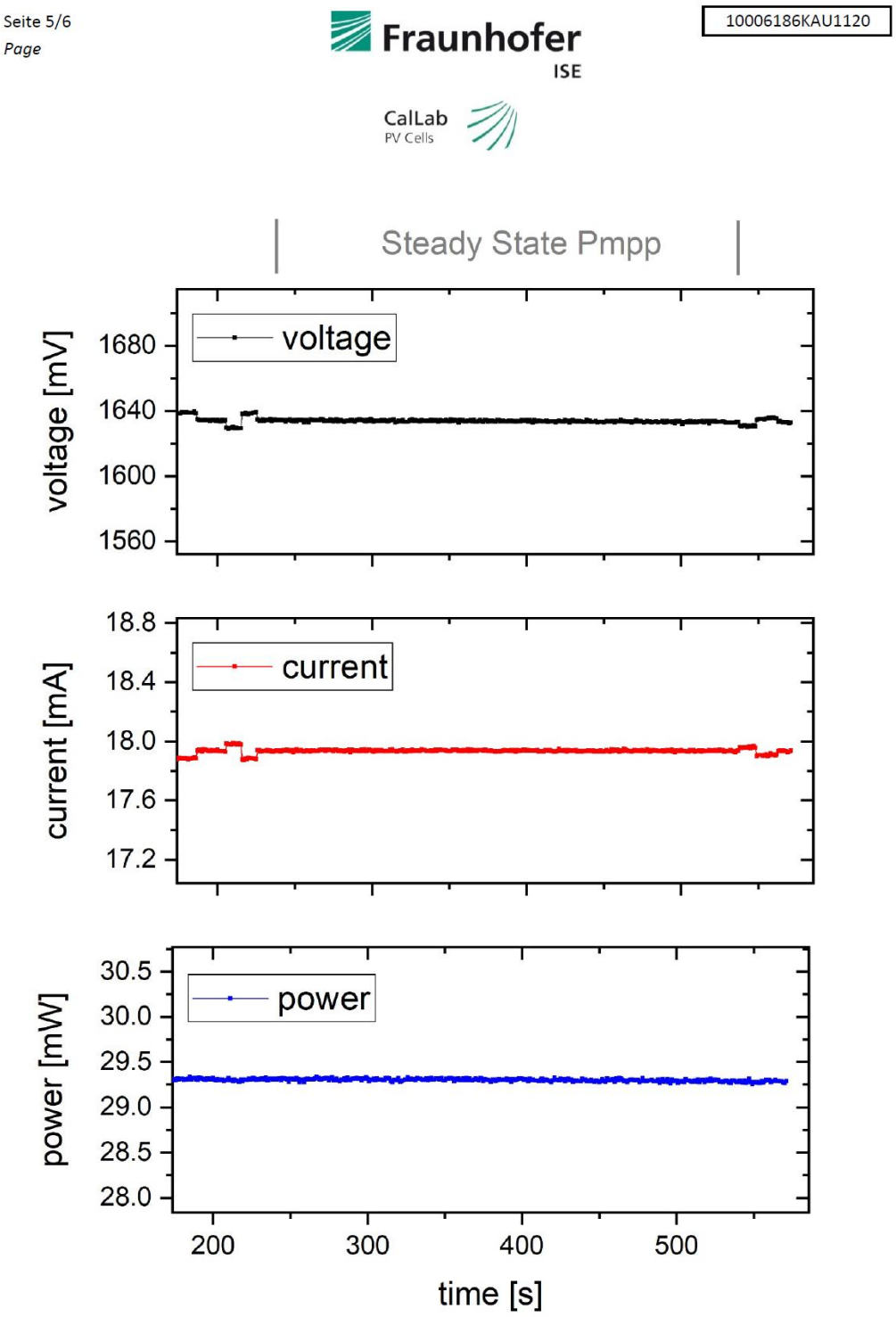

Fig. S21. Certification report by Fraunhofer Institute of Solar Energy (ISE). The area is (1.0002 ± 0.0062) cm^2. Date of calibration: 24.09.2021.

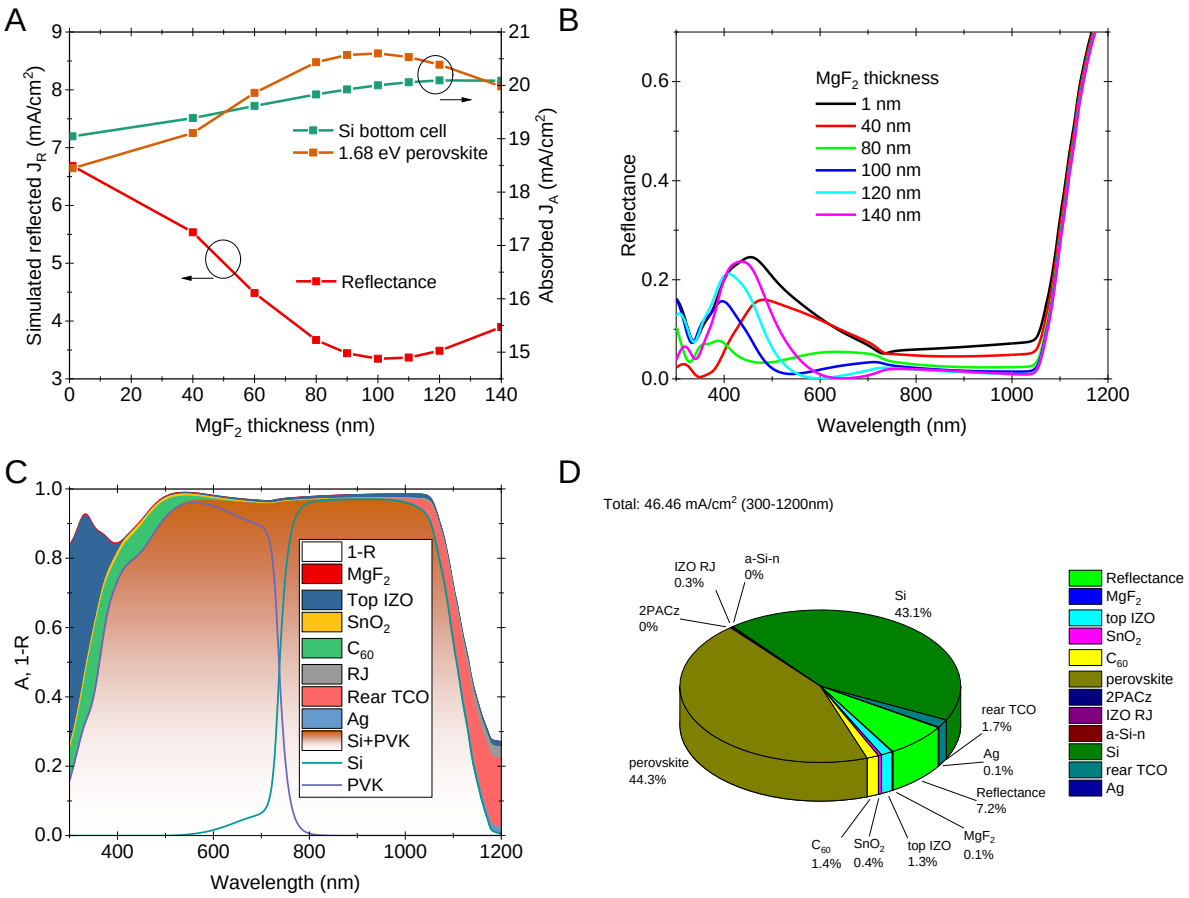

Fig. S22. Optical simulation. (A) The simulated integrated current density of reflectance R and absorbance A based on AM1.5G spectra over 300-1200 nm under different anti-reflectance coating (MgF_x) layer thickness. (B) Simulated reflectance curves of our monolithic perovskite/Si tandem devices. (C) Optical loss analysis of our optimized monolithic perovskite/Si tandem under 100 nm MgF_x layer. (D) The ratio of integration current density for reflectance R and absorbance A in (C). The shadow loss caused by the front metal finger was not considered in the simulation.

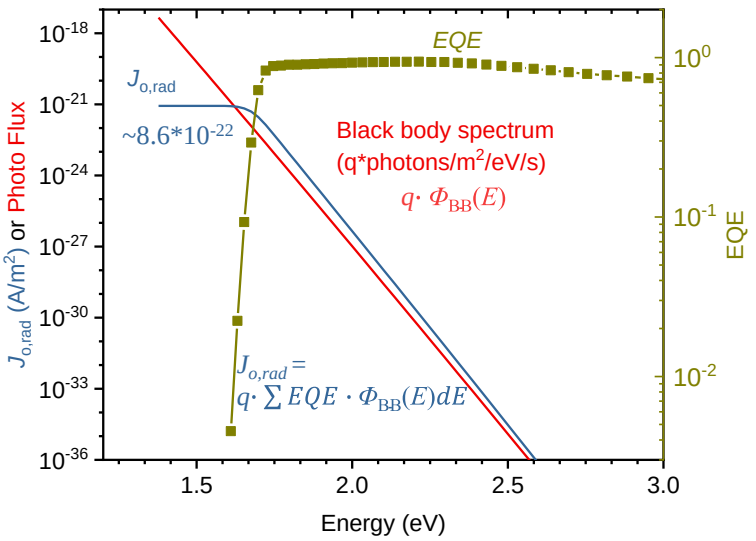

Fig. S23. Calculation of the dark radiative recombination current density $J_{0,rad}$ and the EQE of perovskite subcell on a tandem.

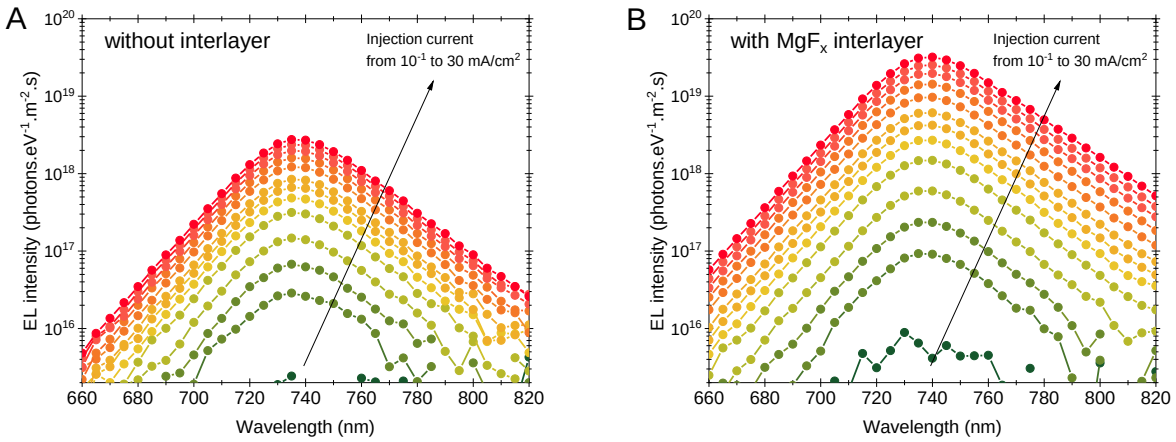

Fig. S24. Intensity-dependent absolute EL spectra of the perovskite subcell.

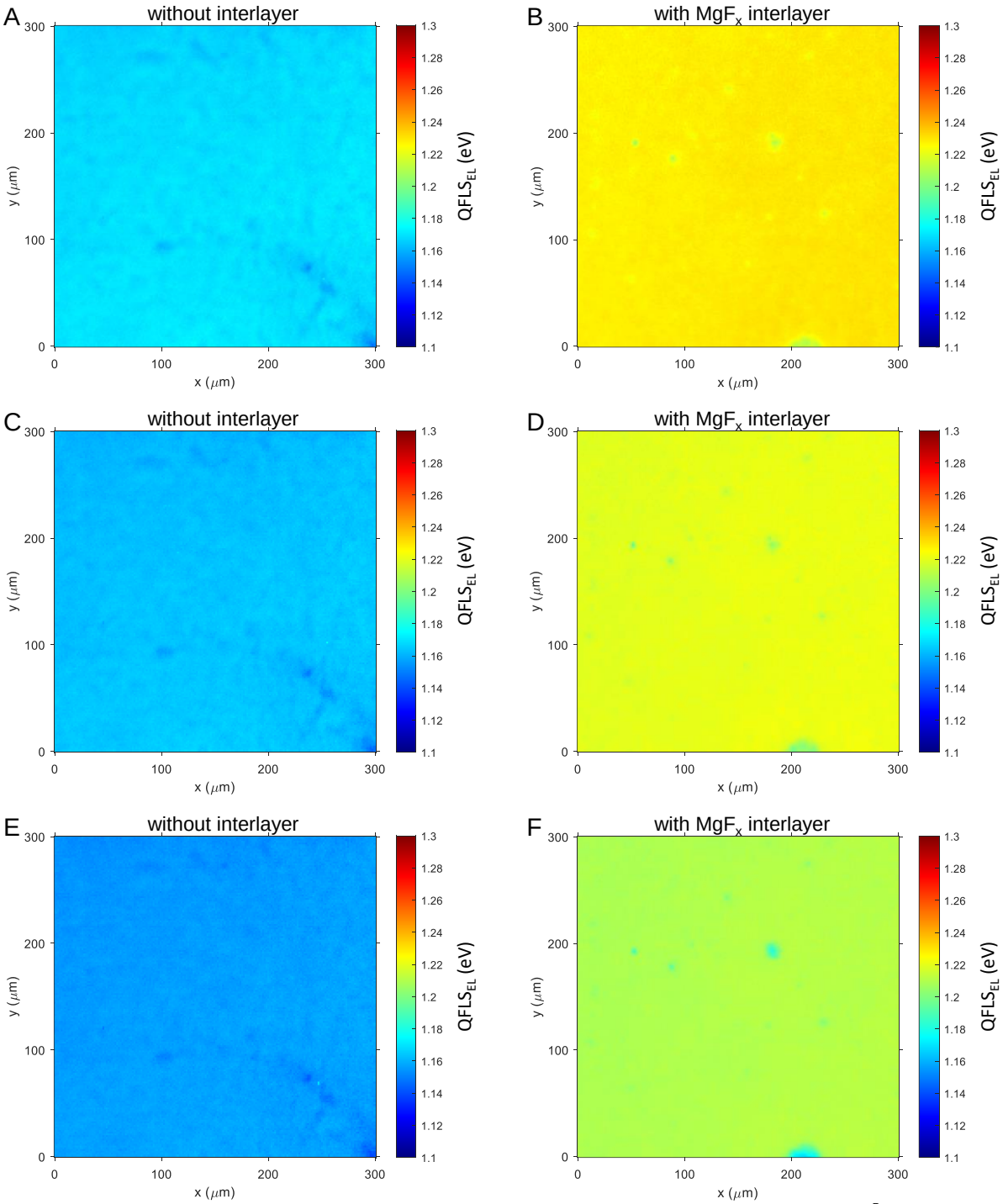

Fig. S25. *QFLS*$_{EL}$ mapping under different injection current: (A, B) 22 mA/cm^2, (C, D) 22 mA/cm^2 , (E, F) 22 mA/cm^2.

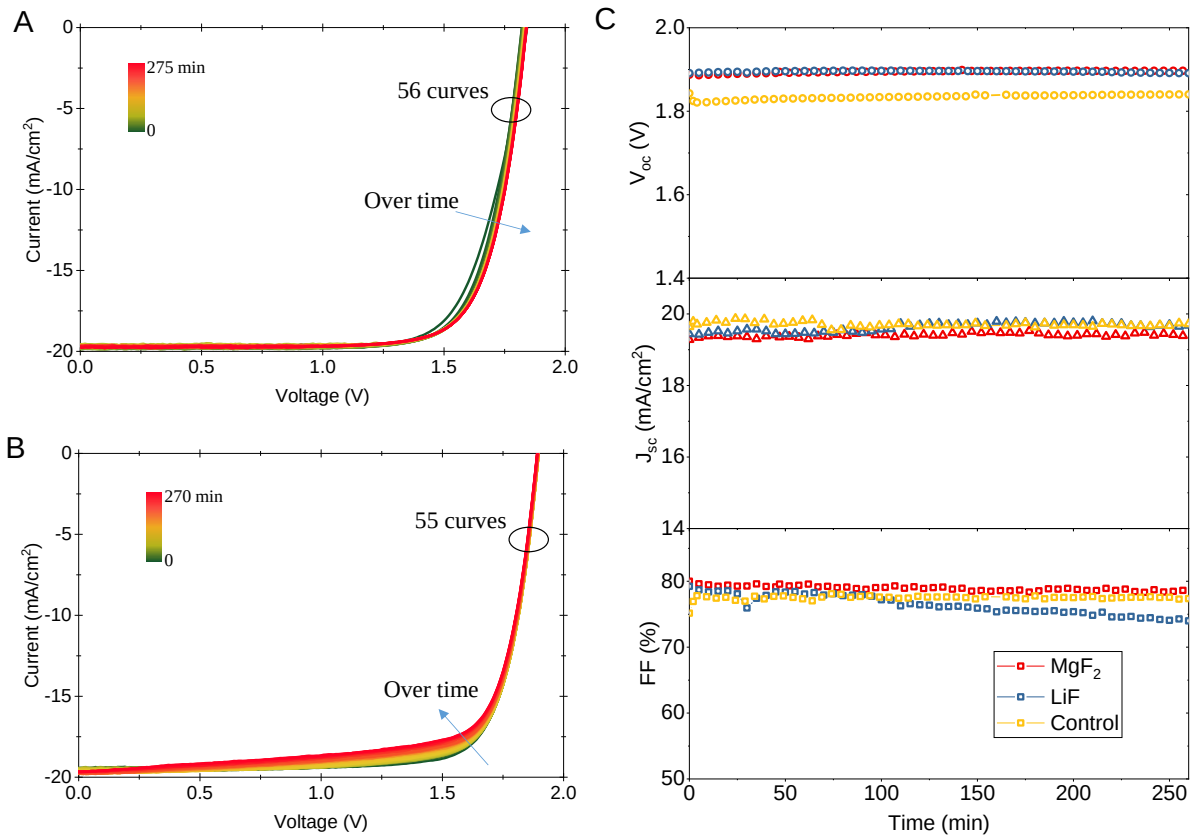

Fig. S26. Air stability tests. (A, B) I-V curves of the tandem devices (A) without fluoride, and (B) with LiF interlayer under continual AM 1.5G illumination. (C) Evolution of V_{oc}, *FF* and J_{sc}.

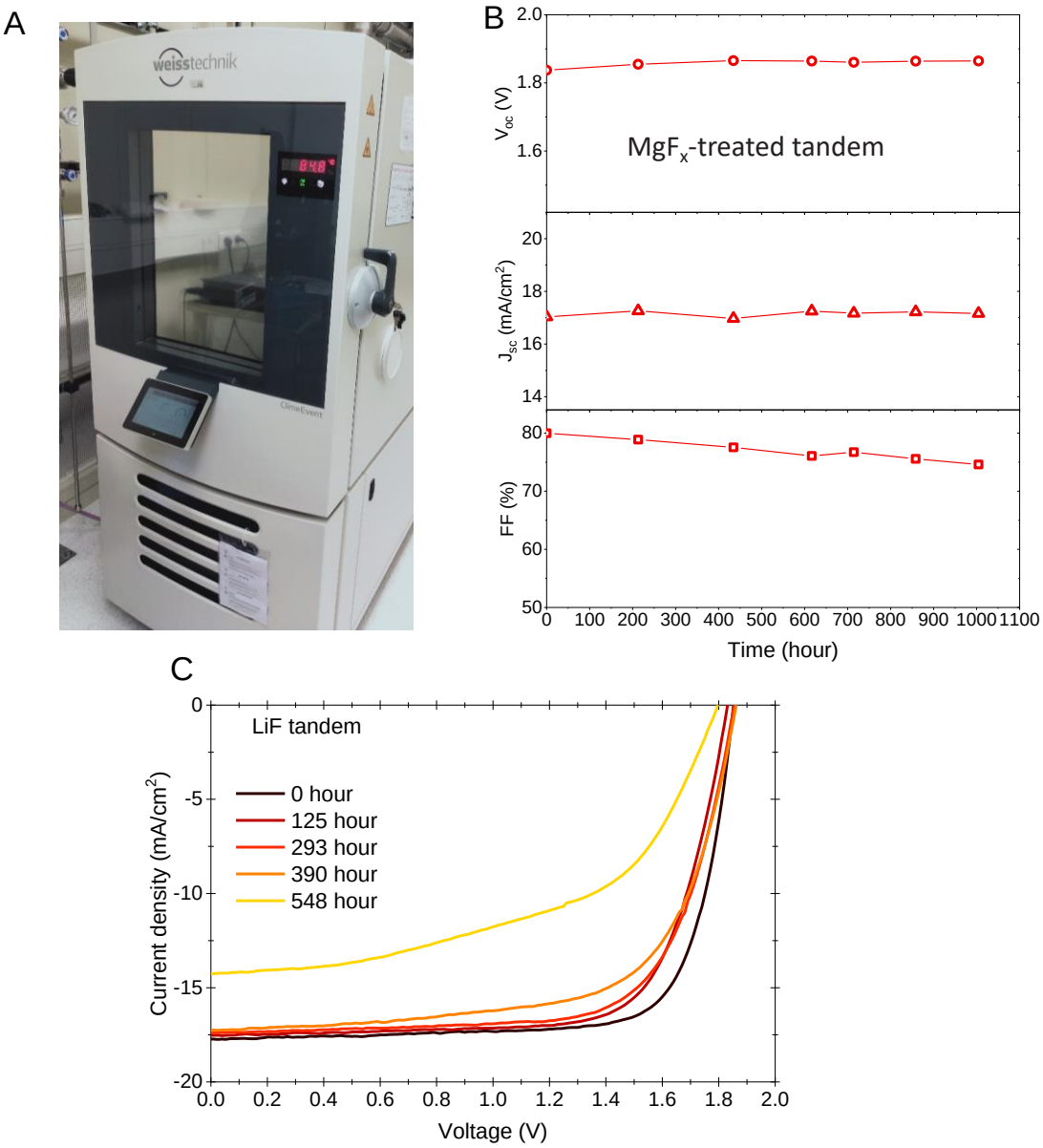

Fig. S27. Damp heat tests. (A) Photo of test equipment which can provide damp heat environment of 85 °C and 85% RH. (B) Evolution of V_{oc}, *FF* and J_{sc} of MgF_x-treated tandem in Fig. 4C. (C) J-V curves of the LiF-treated tandem device during damp heat tests. The tandem device was taken out for IV measurement under standard AM1.5G spectra from time to time. During measurement, a black aperture mask was used. After IV measurement, the device was put back immediately to the damp heat chamber. Since the tandem was encapsulated with thick cover glass and TPU encapsulant (see Fig. 4C inset), the current density of the encapsulated tandem is relatively lower compared with the bare tandem, due to the reflectance loss.

Reference and Notes

1. T. Leijtens, K. A. Bush, R. Prasanna, M. D. McGehee, Opportunities and challenges for tandem solar cells using metal halide perovskite semiconductors. *Nat. Energy* **3**, 828-838 (2018). doi:10.1038/s41560-018-0190-4
2. R. Wang, T. Huang, J. Xue, J. Tong, K. Zhu, Y. Yang, Prospects for metal halide perovskite-based tandem solar cells. *Nat. Photonics* **15**, 411-425 (2021). doi:10.1038/s41566-021-00809-8
3. H. Shen, S. T. Omelchenko, D. A. Jacobs, S. Yalamanchili, Y. Wan, D. Yan, P. Phang, T. Duong, Y. Wu, Y. Yin, C. Samundsett, J. Peng, N. Wu, T. P. White, G. G. Andersson, N. S. Lewis, K. R. Catchpole, In situ recombination junction between p-Si and TiO_2 enables high-efficiency monolithic perovskite/Si tandem cells. *Sci. Adv.* **4**, eaau9711 (2018). doi:10.1126/sciadv.aau9711
4. E. Aydin, J. Liu, E. Ugur, R. Azmi, G. T. Harrison, Y. Hou, B. Chen, S. Zhumagali, M. De Bastiani, M. C. Wang, W. Raja, T. G. Allen, A. U. Rehman, A. S. Subbiah, M. Babics, A. Babayigit, F. H. Isikgor, K. Wang, E. Van Kerschaver, L. Tsetseris, E. H. Sargent, F. Laquai, S. De Wolf, Ligand-bridged charge extraction and enhanced quantum efficiency enable efficient n-i-p perovskite/silicon tandem solar cells. *Energy Environ. Sci.* **14**, 4377-4390 (2021). doi:10.1039/d1ee01206a
5. A. Richter, M. Hermle, S. W. Glunz, Reassessment of the Limiting Efficiency for Crystalline Silicon Solar Cells. *IEEE Journal of Photovoltaics* **3**, 1184-1191 (2013). doi:10.1109/jphotov.2013.2270351
6. B. Chen, Z. Yu, K. Liu, X. Zheng, Y. Liu, J. Shi, D. Spronk, P. N. Rudd, Z. Holman, J. Huang, Grain Engineering for Perovskite/Silicon Monolithic Tandem Solar Cells with Efficiency of 25.4%. *Joule* **3**, 177-190 (2019). doi:10.1016/j.joule.2018.10.003
7. J. P. Mailoa, C. D. Bailie, E. C. Johlin, E. T. Hoke, A. J. Akey, W. H. Nguyen, M. D. McGehee, T. Buonassisi, A 2-terminal perovskite/silicon multijunction solar cell enabled by a silicon tunnel junction. *Appl. Phys. Lett.* **106**, 121105 (2015). doi:10.1063/1.4914179
8. B. Chen, Z. S. J. Yu, S. Manzoor, S. Wang, W. Weigand, Z. H. Yu, G. Yang, Z. Y. Ni, X. Z. Dai, Z. C. Holman, J. S. Huang, Blade-Coated Perovskites on Textured Silicon for 26%-Efficient Monolithic Perovskite/Silicon Tandem Solar Cells. *Joule* **4**, 850-864 (2020). doi:10.1016/j.joule.2020.01.008
9. J. Liu, E. Aydin, J. Yin, M. De Bastiani, F. H. Isikgor, A. U. Rehman, E. Yengel, E. Ugur, G. T. Harrison, M. Wang, Y. Gao, J. I. Khan, M. Babics, T. G. Allen, A. S. Subbiah, K. Zhu, X. Zheng, W. Yan, F. Xu, M. F. Salvador, O. M. Bakr, T. D. Anthopoulos, M. Lanza, O. F. Mohammed, F. Laquai, S. De Wolf, 28.2%-efficient, outdoor-stable perovskite/silicon tandem solar cell. *Joule* **5**, 3169-3186 (2021). doi:10.1016/j.joule.2021.11.003
10. M. Jošt, E. Köhnen, A. B. Morales-Vilches, B. Lipovšek, K. Jäger, B. Macco, A. Al-Ashouri, J. Krč, L. Korte, B. Rech, R. Schlatmann, M. Topič, B. Stannowski, S. Albrecht, Textured interfaces in monolithic perovskite/silicon tandem solar cells: advanced light

management for improved efficiency and energy yield. *Energy Environ. Sci.* **11**, 3511-3523 (2018). doi:10.1039/c8ee02469c

11. F. Sahli, J. Werner, B. A. Kamino, M. Brauninger, R. Monnard, B. Paviet-Salomon, L. Barraud, L. Ding, J. J. Diaz Leon, D. Sacchetto, G. Cattaneo, M. Despeisse, M. Boccard, S. Nicolay, Q. Jeangros, B. Niesen, C. Ballif, Fully textured monolithic perovskite/silicon tandem solar cells with 25.2% power conversion efficiency. *Nat. Mater.* **17**, 820-826 (2018). doi:10.1038/s41563-018-0115-4
12. R. Santbergen, R. Mishima, T. Meguro, M. Hino, H. Uzu, J. Blanker, K. Yamamoto, M. Zeman, Minimizing optical losses in monolithic perovskite/c-Si tandem solar cells with a flat top cell. *Opt Express* **24**, A1288-1299 (2016). doi:10.1364/OE.24.0A1288
13. K. A. Bush, A. F. Palmstrom, Z. J. Yu, M. Boccard, R. Cheacharoen, J. P. Mailoa, D. P. McMeekin, R. L. Z. Hoye, C. D. Bailie, T. Leijtens, I. M. Peters, M. C. Minichetti, N. Rolston, R. Prasanna, S. Sofia, D. Harwood, W. Ma, F. Moghadam, H. J. Snaith, T. Buonassisi, Z. C. Holman, S. F. Bent, M. D. McGehee, 23.6%-efficient monolithic perovskite/silicon tandem solar cells with improved stability. *Nat. Energy* **2**, 17009 (2017). doi:10.1038/nenergy.2017.9
14. D. Kim, H. J. Jung, I. J. Park, B. W. Larson, S. P. Dunfield, C. Xiao, J. Kim, J. Tong, P. Boonmongkolras, S. G. Ji, F. Zhang, S. R. Pae, M. Kim, S. B. Kang, V. Dravid, J. J. Berry, J. Y. Kim, K. Zhu, D. H. Kim, B. Shin, Efficient, stable silicon tandem cells enabled by anion-engineered wide-bandgap perovskites. *Science* **368**, 155-160 (2020). doi:10.1126/science.aba3433
15. J. Xu, C. C. Boyd, Z. J. Yu, A. F. Palmstrom, D. J. Witter, B. W. Larson, R. M. France, J. Werner, S. P. Harvey, E. J. Wolf, W. Weigand, S. Manzoor, M. van Hest, J. J. Berry, J. M. Luther, Z. C. Holman, M. D. McGehee, Triple-halide wide-band gap perovskites with suppressed phase segregation for efficient tandems. *Science* **367**, 1097-1104 (2020). doi:10.1126/science.aaz5074
16. Y. Hou, E. Aydin, M. De Bastiani, C. Xiao, F. H. Isikgor, D.-J. Xue, B. Chen, H. Chen, B. Bahrami, A. H. Chowdhury, A. Johnston, S.-W. Baek, Z. Huang, M. Wei, Y. Dong, J. Troughton, R. Jalmood, A. J. Mirabelli, T. G. Allen, E. Van Kerschaver, M. I. Saidaminov, D. Baran, Q. Qiao, K. Zhu, S. De Wolf, E. H. Sargent, Efficient tandem solar cells with solution-processed perovskite on textured crystalline silicon. *Science* **367**, 1135-1140 (2020). doi:10.1126/science.aaz3691
17. S. Zhumagali, F. H. Isikgor, P. Maity, J. Yin, E. Ugur, M. De Bastiani, A. S. Subbiah, A. J. Mirabelli, R. Azmi, G. T. Harrison, J. Troughton, E. Aydin, J. Liu, T. Allen, A. u. Rehman, D. Baran, O. F. Mohammed, S. De Wolf, Linked Nickel Oxide/Perovskite Interface Passivation for High-Performance Textured Monolithic Tandem Solar Cells. *Adv. Energy Mater.* **11**, 2101662 (2021). doi:10.1002/aenm.202101662
18. A. Al-Ashouri, A. Magomedov, M. Roß, M. Jošt, M. Talaikis, G. Chistiakova, T. Bertram, J. A. Márquez, E. Köhnen, E. Kasparavičius, S. Levcenco, L. Gil-Escrig, C. J. Hages, R. Schlatmann, B. Rech, T. Malinauskas, T. Unold, C. A. Kaufmann, L. Korte, G. Niaura, V. Getautis, S. Albrecht, Conformal monolayer contacts with lossless interfaces for perovskite single junction and monolithic tandem solar cells. *Energy Environ. Sci.* **12**, 3356-3369 (2019). doi:10.1039/c9ee02268f
19. A. Al-Ashouri, E. Kohnen, B. Li, A. Magomedov, H. Hempel, P. Caprioglio, J. A. Marquez, A. B. Morales Vilches, E. Kasparavicius, J. A. Smith, N. Phung, D. Menzel, M. Grischek, L. Kegelmann, D. Skroblin, C. Gollwitzer, T. Malinauskas, M. Jost, G. Matic,

B. Rech, R. Schlatmann, M. Topic, L. Korte, A. Abate, B. Stannowski, D. Neher, M. Stolterfoht, T. Unold, V. Getautis, S. Albrecht, Monolithic perovskite/silicon tandem solar cell with >29% efficiency by enhanced hole extraction. *Science* **370**, 1300-1309 (2020). doi:10.1126/science.abd4016

20. E. L. Unger, L. Kegelmann, K. Suchan, D. Sörell, L. Korte, S. Albrecht, Roadmap and roadblocks for the band gap tunability of metal halide perovskites. *J. Mater. Chem. A* **5**, 11401-11409 (2017). doi:10.1039/c7ta00404d
21. F. Peña-Camargo, P. Caprioglio, F. Zu, E. Gutierrez-Partida, C. M. Wolff, K. Brinkmann, S. Albrecht, T. Riedl, N. Koch, D. Neher, M. Stolterfoht, Halide Segregation versus Interfacial Recombination in Bromide-Rich Wide-Gap Perovskite Solar Cells. *ACS Energy Lett.* **5**, 2728-2736 (2020). doi:10.1021/acsenergylett.0c01104
22. M. Stolterfoht, P. Caprioglio, C. M. Wolff, J. A. Márquez, J. Nordmann, S. Zhang, D. Rothhardt, U. Hörmann, Y. Amir, A. Redinger, L. Kegelmann, F. Zu, S. Albrecht, N. Koch, T. Kirchartz, M. Saliba, T. Unold, D. Neher, The impact of energy alignment and interfacial recombination on the internal and external open-circuit voltage of perovskite solar cells. *Energy Environ. Sci.* **12**, 2778-2788 (2019). doi:10.1039/c9ee02020a
23. J. S. Luo, J. X. Xia, H. Yang, L. L. Chen, Z. Q. Wan, F. Han, H. A. Malik, X. H. Zhu, C. Y. Jia, Toward high-efficiency, hysteresis-less, stable perovskite solar cells: unusual doping of a hole-transporting material using a fluorine-containing hydrophobic Lewis acid. *Energy Environ. Sci.* **11**, 2035-2045 (2018). doi:10.1039/c8ee00036k
24. S. G. Kim, T. H. Le, T. de Monfreid, F. Goubard, T. T. Bui, N. G. Park, Capturing Mobile Lithium Ions in a Molecular Hole Transporter Enhances the Thermal Stability of Perovskite Solar Cells. *Adv. Mater.* **33**, e2007431 (2021). doi:10.1002/adma.202007431
25. Z. Li, C. Xiao, Y. Yang, S. P. Harvey, D. H. Kim, J. A. Christians, M. Yang, P. Schulz, S. U. Nanayakkara, C.-S. Jiang, J. M. Luther, J. J. Berry, M. C. Beard, M. M. Al-Jassim, K. Zhu, Extrinsic ion migration in perovskite solar cells. *Energy Environ. Sci.* **10**, 1234-1242 (2017). doi:10.1039/c7ee00358g
26. Z. Liu, J. Siekmann, B. Klingebiel, U. Rau, T. Kirchartz, Interface Optimization via Fullerene Blends Enables Open-Circuit Voltages of 1.35 V in $CH_3NH_3Pb(I_{0.8}Br_{0.2})_3$ Solar Cells. *Adv. Energy Mater.* **11**, 2003386 (2021). doi:10.1002/aenm.202003386
27. Q. Jiang, Y. Zhao, X. Zhang, X. Yang, Y. Chen, Z. Chu, Q. Ye, X. Li, Z. Yin, J. You, Surface passivation of perovskite film for efficient solar cells. *Nat. Photonics* **13**, 460-466 (2019). doi:10.1038/s41566-019-0398-2
28. E. Aydin, C. Altinkaya, Y. Smirnov, M. A. Yaqin, K. P. S. Zanoni, A. Paliwal, Y. Firdaus, T. G. Allen, T. D. Anthopoulos, H. J. Bolink, M. Morales-Masis, S. De Wolf, Sputtered transparent electrodes for optoelectronic devices: Induced damage and mitigation strategies. *Matter* **4**, 3549-3584 (2021). doi:10.1016/j.matt.2021.09.021
29. J. Endres, D. A. Egger, M. Kulbak, R. A. Kerner, L. Zhao, S. H. Silver, G. Hodes, B. P. Rand, D. Cahen, L. Kronik, A. Kahn, Valence and Conduction Band Densities of States of Metal Halide Perovskites: A Combined Experimental-Theoretical Study. *J. Phys. Chem. Lett.* **7**, 2722-2729 (2016). doi:10.1021/acs.jpclett.6b00946
30. L. Canil, T. Cramer, B. Fraboni, D. Ricciarelli, D. Meggiolaro, A. Singh, M. Liu, M. Rusu, C. M. Wolff, N. Phung, Q. Wang, D. Neher, T. Unold, P. Vivo, A. Gagliardi, F. De Angelis, A. Abate, Tuning halide perovskite energy levels. *Energy Environ. Sci.* **14**, 1429-1438 (2021). doi:10.1039/d0ee02216k

31. P. Schulz, L. L. Whittaker-Brooks, B. A. MacLeod, D. C. Olson, Y.-L. Loo, A. Kahn, Electronic Level Alignment in Inverted Organometal Perovskite Solar Cells. *Adv. Mater. Interfaces* **2**, 1400532 (2015). doi:10.1002/admi.201400532
32. Y. Wan, C. Samundsett, J. Bullock, T. Allen, M. Hettick, D. Yan, P. Zheng, X. Zhang, J. Cui, J. McKeon, A. Javey, A. Cuevas, Magnesium Fluoride Electron-Selective Contacts for Crystalline Silicon Solar Cells. *ACS Appl. Mater. Interfaces* **8**, 14671-14677 (2016). doi:10.1021/acsami.6b03599
33. D. W. deQuilettes, S. Koch, S. Burke, R. K. Paranji, A. J. Shropshire, M. E. Ziffer, D. S. Ginger, Photoluminescence Lifetimes Exceeding 8 μs and Quantum Yields Exceeding 30% in Hybrid Perovskite Thin Films by Ligand Passivation. *ACS Energy Lett.* **1**, 438-444 (2016). doi:10.1021/acsenergylett.6b00236
34. M. Stolterfoht, M. Grischek, P. Caprioglio, C. M. Wolff, E. Gutierrez-Partida, F. Pena-Camargo, D. Rothhardt, S. Zhang, M. Raoufi, J. Wolansky, M. Abdi-Jalebi, S. D. Stranks, S. Albrecht, T. Kirchartz, D. Neher, How To Quantify the Efficiency Potential of Neat Perovskite Films: Perovskite Semiconductors with an Implied Efficiency Exceeding 28. *Adv. Mater.* **32**, e2000080 (2020). doi:10.1002/adma.202000080
35. F. Bussolotti, J. Yang, M. Hiramoto, T. Kaji, S. Kera, N. Ueno, Direct detection of density of gap states in C_{60} single crystals by photoemission spectroscopy. *Phys. Rev. B* **92**, 115102 (2015). doi:10.1103/PhysRevB.92.115102
36. Y. Shao, Y. Yuan, J. Huang, Correlation of energy disorder and open-circuit voltage in hybrid perovskite solar cells. *Nat. Energy* **1**, 15001 (2016). doi:10.1038/nenergy.2015.1
37. M. Sajjad, X. Yang, P. Altermatt, N. Singh, U. Schwingenschlögl, S. De Wolf, Metal-induced gap states in passivating metal/silicon contacts. *Appl. Phys. Lett.* **114**, (2019). doi:10.1063/1.5066423
38. J. Robertson, Band offsets of wide-band-gap oxides and implications for future electronic devices. *Journal of Vacuum Science & Technology B: Microelectronics and Nanometer Structures Processing, Measurement, and Phenomena* **18**, 1785-1791 (2000). doi:10.1116/1.591472
39. S. M. Park, A. Abtahi, A. M. Boehm, K. R. Graham, Surface Ligands for Methylammonium Lead Iodide Films: Surface Coverage, Energetics, and Photovoltaic Performance. *ACS Energy Lett.* **5**, 799-806 (2020). doi:10.1021/acsenergylett.0c00054
40. J.-P. Yang, F. Bussolotti, S. Kera, N. Ueno, Origin and role of gap states in organic semiconductor studied by UPS: as the nature of organic molecular crystals. *Journal of Physics D: Applied Physics* **50**, (2017). doi:10.1088/1361-6463/aa840f
41. C. A. Hoffman, K. Jarašiūnas, H. J. Gerritsen, A. V. Nurmikko, Measurement of surface recombination velocity in semiconductors by diffraction from picosecond transient free-carrier gratings. *Appl. Phys. Lett.* **33**, 536-539 (1978). doi:10.1063/1.90428
42. Y. Yang, M. Yang, David T. Moore, Y. Yan, Elisa M. Miller, K. Zhu, Matthew C. Beard, Top and bottom surfaces limit carrier lifetime in lead iodide perovskite films. *Nat. Energy* **2**, 16207 (2017). doi:10.1038/nenergy.2016.207
43. F. Lang, E. Köhnen, J. Warby, K. Xu, M. Grischek, P. Wagner, D. Neher, L. Korte, S. Albrecht, M. Stolterfoht, Revealing Fundamental Efficiency Limits of Monolithic Perovskite/Silicon Tandem Photovoltaics through Subcell Characterization. *ACS Energy Lett.* **6**, 3982-3991 (2021). doi:10.1021/acsenergylett.1c01783
44. F. H. Isikgor, F. Furlan, J. Liu, E. Ugur, M. K. Eswaran, A. S. Subbiah, E. Yengel, M. De Bastiani, G. T. Harrison, S. Zhumagali, C. T. Howells, E. Aydin, M. Wang, N. Gasparini,

T. G. Allen, A. u. Rehman, E. Van Kerschaver, D. Baran, I. McCulloch, T. D. Anthopoulos, U. Schwingenschlögl, F. Laquai, S. De Wolf, Concurrent cationic and anionic perovskite defect passivation enables 27.4% perovskite/silicon tandems with suppression of halide segregation. *Joule* **5**, 1566-1586 (2021). doi:10.1016/j.joule.2021.05.013

45. J. P. Perdew, K. Burke, M. Ernzerhof, Generalized Gradient Approximation Made Simple. *Phys. Rev. Lett.* **77**, 3865-3868 (1996). doi:10.1103/PhysRevLett.77.3865
46. G. Kresse, D. Joubert, From ultrasoft pseudopotentials to the projector augmented-wave method. *Phys. Rev. B* **59**, 1758-1775 (1999). doi:10.1103/PhysRevB.59.1758
47. Aron Walsh, elds22, F. Brivio, J. M. Frost, WMD-group/hybrid-perovskites: Collection 1 (v1.0). Zenodo. (2019). doi:10.5281/zenodo.2641358
48. N. Li, S. Tao, Y. Chen, X. Niu, C. K. Onwudinanti, C. Hu, Z. Qiu, Z. Xu, G. Zheng, L. Wang, Y. Zhang, L. Li, H. Liu, Y. Lun, J. Hong, X. Wang, Y. Liu, H. Xie, Y. Gao, Y. Bai, S. Yang, G. Brocks, Q. Chen, H. Zhou, Cation and anion immobilization through chemical bonding enhancement with fluorides for stable halide perovskite solar cells. *Nat. Energy* **4**, 408-415 (2019). doi:10.1038/s41560-019-0382-6
49. S. Grimme, J. Antony, S. Ehrlich, H. Krieg, A consistent and accurate ab initio parametrization of density functional dispersion correction (DFT-D) for the 94 elements H-Pu. *The Journal of Chemical Physics* **132**, 154104 (2010). doi:10.1063/1.3382344
50. R. A. Jishi, O. B. Ta, A. A. Sharif, Modeling of Lead Halide Perovskites for Photovoltaic Applications. *J. Phys. Chem. C* **118**, 28344-28349 (2014). doi:10.1021/jp5050145
51. K.-H. Chew, R. Kuwahara, K. Ohno, Electronic structure of Li+@C60 adsorbed on methyl-ammonium lead iodide perovskite CH3NH3PbI3 surfaces. *Materials Advances* **3**, 290-299 (2022). doi:10.1039/D1MA00741F
52. G. Kresse, J. Furthmüller, Efficiency of ab-initio total energy calculations for metals and semiconductors using a plane-wave basis set. *Computational Materials Science* **6**, 15-50 (1996). doi:10.1016/0927-0256(96)00008-0
53. K. Momma, F. Izumi, VESTA 3 for three-dimensional visualization of crystal, volumetric and morphology data. *Journal of Applied Crystallography* **44**, 1272-1276 (2011). doi:10.1107/S0021889811038970
54. A. M. Ganose, A. J. Jackson, D. O. Scanlon, sumo: Command-line tools for plotting and analysis of periodic *ab initio* calculations. *Journal of Open Source Software* **3**, (2018). doi:10.21105/joss.00717
55. V. Wang, N. Xu, J.-C. Liu, G. Tang, W.-T. Geng, VASPKIT: A user-friendly interface facilitating high-throughput computing and analysis using VASP code. *Computer Physics Communications* **267**, 108033 (2021). doi:10.1016/j.cpc.2021.108033
56. Q. h. Wu, S. q. Wu, C. I. Pakes, Impact of Surface Dipole on Resonant Electron Injection in Scanning Tunneling Spectroscopy. *Chinese Journal of Chemical Physics* **26**, 393-397 (2013). doi:10.1063/1674-0068/26/04/393-397